Impact of Josephson Junction Array modes on Fluxonium Readout

Shraddha Singh[1, 2, 3, *] Gil Refael,[3, 4] Aashish Clerk,[5, 3] and Emma Rosenfeld[3, †]

[1]*Department of Applied Physics and Physics, Yale University, New Haven, Connecticut 06511, USA*
[2]*Yale Quantum Institute, Yale University, New Haven, Connecticut 06511, USA*
[3]*AWS Center for Quantum Computing, Pasadena, CA 91125, USA*
[4]*Institute for Quantum Information and Matter,*
California Institute of Technology, Pasadena, CA 91125
[5]*Pritzker School of Molecular Engineering, University of Chicago, Chicago, Illinois 60637, USA*
(Dated: November 10, 2024)

Dispersive readout of superconducting qubits is often limited by non-ideal backaction effects in which the readout drive induces unwanted transitions between qubit levels. While there is a growing understanding of such effects in transmon qubits, the case of highly nonlinear fluxonium qubits is more complex. We theoretically analyze measurement-induced state transitions (MIST) during the dispersive readout of a fluxonium qubit, focusing on a new mechanism: the possibility of transitions where the drive simultaneously excites an internal mode of the Josephson junction array in the fluxonium circuit, while also causing a qubit transition. Using an adiabatic Floquet approach, we show that these new kinds of MIST processes are relevant at particular values of realistic circuit parameters and relatively low readout drive powers. As we show, they can also contribute to excess qubit dephasing even after a measurement is complete. In a study of mitigation strategies, we highlight readout frequency choices which avoid p-MIST, and analyze the dependency of qubit-parasitic mode coupling on different circuit parameters. Our results underscore the impact of parasitic modes on qubit performance in highly anharmonic superconducting circuits, if they are not carefully treated during circuit design.

I. INTRODUCTION

The fluxonium superconducting qubit, based on a Josephson junction shunted by a capacitor and a large inductance, has emerged as an extremely promising platform for quantum information. It exhibits extremely long lifetimes [1–4], and both single [5] and two-qubit gates [6, 7] have been demonstrated with high fidelity, with potential room for even further improvements [8–12]. The inductive shunt is a crucial part of the fluxonium circuit, with the most common realization being a Josephson junction array (JJA); in regimes where internal array modes are not excited, the JJA can act as a linear superinductance (see e.g. [13, 14]).

In addition to coherence and the ability to do high-fidelity gates, the ability to make fast and efficient measurements is crucial to any qubit platform. Similar to other superconducting qubits, dispersive readout (using a driven readout resonator) has been the standard choice for fluxonium readout (see e.g. [5]). While such measurement schemes should ideally be quantum non-demolition (QND) [15], some experiments have reported non-QND backaction (either enhanced relaxation or transitions to non-computational states) during fluxonium readout [6, 16–18]. This is similar to the situation with dispersive readout with more standard transmon qubits, where similar effects have long been seen. Recent theoretical work on driven transmon qubits has provided strong insights into these so-called measurement-induced state transitions (MIST), showing that multi-photon transitions can lead to resonant excitation of the transmon to higher levels (see e.g. [19–24]).
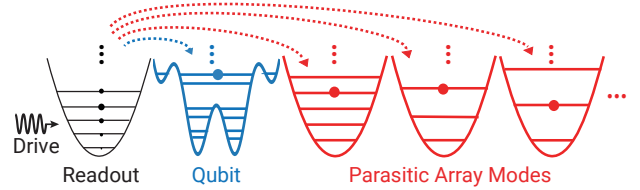
FIG. 1. A parasitic effect where energy in a coherent state of the driven readout mode (black) excites extraneous linear modes (red) and the nonlinear qubit mode (blue) simultaneously.

Given that similar MIST-like effects have been seen in fluxonium qubits, it is only natural to want a similar theoretical understanding of the relevant mechanisms, to ultimately find means for suppressing such effects. There are of course significant differences between fluxonium and the transmon, which will significantly alter MIST physics. For example, the enhanced nonlinearity can dramatically change the number and likelihood of potential transitions [20, 25]. In this work, we provide a comprehensive analysis of another new MIST mechanism in fluxonium: additional MIST transitions of the qubit that arise due to the internal modes of the JJA in the fluxonium circuit (see Fig. 1). We show that for realistic parameters and drive powers, deleterious resonant processes that simultaneously excite the qubit and an internal mode can indeed occur; we term these processes parasitic-mode induced state transitions (p-MIST). One can view this as an example of an even more general problem: how is MIST physics modified in the presence of a structured environment?

We focus on a heavy fluxonium qubit operated at its flux sweet spot (c.f. Fig. 2) and study MIST effects keeping the coupling to the most relevant JJA internal modes. Similar to studies of MIST in transmons [22, 23], we treat the readout as an effective

FIG. 2. (a) Fluxonium readout circuit. The color scheme shows primary components that correspond to various modes, shown in Fig. 1 when a JJA fluxonium circuit is connected to a readout resonator (R). The subscripts p, j denote components of the phase-slip junction and the JJA, respectively. This circuit shows coupling capacitances (C_c), readout frequency parameters $(\omega_r = 1/\sqrt{L_R C_R})$, parasitic ground capacitances in JJA $(C_{g,j})$ and next to the phase-slip junction $(C_{g,p})$. The differential capacitance C adjusts the charging energy of the qubit mode (see Table II). (b) Fluxonium mode energy levels in units of h, with the highlighted area showing the first three levels essential for certain readout schemes [5]. (c) Parasitic mode frequencies $\omega_\mu/2\pi$. The lowest even mode $\mu = 2$ has the strongest coupling to the qubit (see Fig. 12).

classical drive on the fluxonium-plus-JJA system and use an adiabatic Floquet branch analysis to identify dominant MIST processes. We also validate this approach through full-time-dependent simulations. Our work goes beyond simply showing that such processes could be relevant. We discuss how they could provide a mechanism for degrading qubit coherence even after measurements are complete (via dephasing from dispersive couplings to the excited internal modes). We also discuss how alternate circuit designs could be employed to help minimize p-MIST processes, paying special attention to how modifications affect the parasitic mode to qubit coupling strengths. Our analysis here suggests that once one considers readout, parasitic JJA modes introduce additional constraints on the circuit design for highly coherent fluxonium qubits.

The remainder of this article is structured as follows. Sec. II provides an analysis of the full circuit including fluxonium, JJA, and readout resonator. Using a standard harmonic approximation, we derive qubit-parasitic mode couplings strengths, and lower bound parasitic mode effects during readout. Sec. III analyzes readout dynamics, including MIST processes and dephasing from parasitic modes. Sec. IV analyzes the effects of varying coupling strengths on p-MIST, and investigates different ranges of readout frequencies and parasitic mode frequencies using an energy-conservation picture. Finally, in the concluding Sec. V we discuss directions for future work that build upon our analysis.

N	φ_{ext}	E_{J_p}	E_{C_p}	E_C	E_{C_j}	E_{J_j}	$E_{C_{g,j}}$	$E_{C_{g,p}}$	E_c
122	$0.5\Phi_0$	7.30	1.46	17	0.74	60	194	1.94	19.40

TABLE I. Circuit parameters for Fig. 2(a) inspired by Ref. [5]. All energies are given in GHz. Here $\Phi_0 = h/2e$ denotes the magnetic flux quantum. The capacitive energies $E_{C'} = \frac{19.4}{C'(\text{fF})}$ GHz are computed from the corresponding capacitances C'. See Table IV in App. B for the values of capacitances.

II. FLUXONIUM READOUT CIRCUIT

We consider a JJA-fluxonium circuit dispersively coupled to a readout mode as shown in Fig. 2. We chose circuit parameters (as listed in Table I) motivated by recent experiments on heavy fluxonium [5–7]. We also restrict attention to the flux "sweet spot" that maximizes qubit coherence. This choice is also expected to reduce the number of allowed transitions in the circuit, as transitions between parity-conserving states via first-order processes are forbidden in this case. For our parameters, the qubit frequency $(\omega_{01}/2\pi)$ is ~ 30 MHz and the plasmon frequency (i.e. splitting frequency between first and second qubit excited states $\omega_{12}/2\pi$) is ~ 6 GHz (see Table II for a full list of readout parameters).

Our work specifically investigates the role of the JJA, which comprises the inductive shunt of the fluxonium. The array comprises N junctions and $N - 1$ ground capacitances(C_{g_n}) [26]. We neglect disorder effects, and take junction parameters and parasitic ground capacitances to be uniform in the array (i.e. $C_{g_1} = .. = C_{g_N}$). This capacitance value is given by $C_{g,j}$ where the subscript j indicates the parasitic ground capacitance in the JJA [27]. As shown in Fig. 2(a), two additional identical ground capacitances C_{g_0}, C_{g_N} near the phase-slip junctions may have different values compared to those in the interior of the array, i.e. $C_{g_0} = C_{g_N} \equiv C_{g,p} \neq C_{g,j}$. Note that the subscript p indicates the parasitic ground capacitances next to the phase-slip junction.

The JJA fluxonium circuit has N internal degrees of freedom [28, 29]: one qubit mode (ϕ) and $N - 1$ internal modes $(\mu = 1, 2, ..., N - 1)$. These internal modes are coupled via the ground capacitances and are referred to as the "parasitic" modes of the JJA. In our notation, we label the readout mode as r. The charge and flux quadratures of the qubit mode are denoted by $\hat{N}_\phi$ and $\hat{\phi}$ where $[\hat{\phi}, \hat{N}_\phi] = i\hbar$. We simplify the problem by treating all but the qubit mode as harmonic oscillators as assumed in previous works [23, 28, 29]. We expect that this assumption will lower bound the effects of JJA parasitic modes on qubit performance for driven fluxonium circuits. We denote the photon loss and gain operators of the linear modes r, μ using $\hat{a}_r, \hat{a}_\mu$ and $\hat{a}_r^\dagger, \hat{a}_\mu^\dagger$, respectively.

Setting $\hbar = 1$, the Hamiltonian of our fluxonium circuit has the form (see App. A for derivation)

$$\hat{H} = \hat{H}_\phi + \hat{H}_\mu + \hat{H}_r + \hat{H}_{int}, \qquad (1)$$

where the qubit Hamiltonian $\hat{H}_\phi$ (with JJA inductive

Qubit (ϕ) &	$\omega_{01}/2\pi$	$\omega_{12}/2\pi$	$\tilde{E}_c^\phi$	$g_{\phi r}/2\pi$	$\chi_{\phi r}(01)/2\pi$	$\chi_{\phi r}(12)/2\pi$	$\omega_r/2\pi$	$\kappa_r/2\pi$
Readout (r)	30 MHz	6.04 GHz	0.92 GHz	25.50 MHz	0.18 MHz	0.98 MHz	8.50 GHz	1 MHz
Parasitic-Mode			$g_{\phi\mu}/2\pi$	$g_{\mu r}/2\pi$	$\chi_{\phi\mu}(01)/2\pi$	$\chi_{\phi\mu}(12)/2\pi$	$\omega_\mu/2\pi$	Q_μ
($\mu = 2$)			157 MHz	4.22 MHz	-1.10 MHz	5 MHz	12.06 GHz	10^4

TABLE II. Measurement parameters for qubit mode ϕ, readout mode r and closest even parasitic mode $\mu = 2$. All quantities are derived and computed analytically using circuit parameters listed in Table I (see Apps. A-B for details). **Qubit-Readout Parameters:** (ω_{ij}) qubit $i \to j$ splitting frequency between fluxonium excited states i, j; ($\tilde{E}_c^\phi$) qubit charging energy; ($g_{\phi r}$) qubit-readout coupling; ($\chi_{\phi r}(ij)$) dispersive shift due to readout mode in the two-level ij system; (ω_r) readout mode frequency; (κ_r) decay rate of the readout resonator. **Parasitic-Mode Parameters:** ($g_{\phi\mu}$) qubit-parasitic coupling; ($g_{\mu r}$) parasitic-readout coupling; ($\chi_{\phi\mu}(ij)$) dispersive shift due to parasitic mode μ in the two-level ij system; (ω_μ) mode frequency; and (Q_μ) internal quality factor inspired by [13].

energy $E_L = E_{J_j}/N$) is

$$\hat{H}_\phi/2\pi = 4\tilde{E}_c^\phi \hat{N}_\phi^2 + E_{J_p} \cos\hat{\phi} + E_L \hat{\phi}^2/2, \quad (2)$$

the junction array and readout Hamiltonians are $\hat{H}_\mu = \sum_\mu \omega_\mu \hat{a}_\mu^\dagger \hat{a}_\mu$ and $\hat{H}_r = \omega_r \hat{a}_r^\dagger \hat{a}_r$, respectively. The qubit charging energy $\tilde{E}_c^\phi$ (see Table II) deviates from the target value of $E_c^\phi = 1$ GHz due to parasitic capacitance. The coupling between the three modes is described by the interaction Hamiltonian

$$\hat{H}_{int} = \sum_\mu g_{\phi\mu} \frac{\hat{N}_\phi}{N_{\phi,\mathrm{ZPF}}} (\hat{a}_\mu - \hat{a}_\mu^\dagger)$$
$$- g_{\phi r} \frac{\hat{N}_\phi}{N_{\phi,\mathrm{ZPF}}} (\hat{a}_r - \hat{a}_r^\dagger)$$
$$- \sum_\mu g_{\mu r} (\hat{a}_r - \hat{a}_r^\dagger)(\hat{a}_\mu - \hat{a}_\mu^\dagger). \quad (3)$$

where for our parameters, the zero-point fluctuations of qubit charge $N_{\phi,\mathrm{ZPF}} = 0.36$. Values for all remaining parameters appearing here are given in Table II. Explicit expression for $g_{\phi\mu}$ is discussed in Sec. IV, while expressions for all other variables can be found in App. B.

We verify the conclusion from Ref. [29] that the symmetry of the parallel circuit in Fig. 2(a) prevents coupling between odd parasitic modes (including $\mu = 1$) and other circuit modes. We extend this result to two additional circuits, with different ground circuit configurations, showing qualitatively consistent conclusions across all three circuits in App. A. The circuits yield the same Hamiltonian when the differential capacitance C and coupling capacitance C_c are altered such that qubit frequency and qubit-readout coupling are the same across all three circuits (see Table V in App. A).

We find that the lowest-frequency even parasitic mode $\mu = 2$ has the strongest coupling to the qubit mode (see Fig. 12 in App. B 1); parameters for which are listed in Table II. Moreover, Fig. 12 shows that the $\mu = 2, 4, 6$ parasitic modes couple to the qubit with a strength $g_{\phi\mu}$ that is stronger than the qubit-readout coupling $g_{\phi r}$. This relative behavior between coupling strengths has also been pointed out previously in Ref. [29].

Given the above insights and our stated goal of understanding readout-induced transitions that involve the parasitic modes, in the rest of this work we will focus on the parallel circuit from Fig. 2 using parameters given by Tables I-II in Eq. 1. Further, our description will only retain the strongest coupled parasitic mode $\mu = 2$, along with the qubit and readout resonator. For details on other parasitic modes and their parameters, see App. B 1. Note that for our chosen parameters (see Table I), the qubit couples roughly six times more strongly to the parasitic mode at $\mu = 2$ than it does to the readout r [30]. As we will show, this strong coupling implies that the parasitic mode can play a strong role in measurement-induced state transitions, i.e. the p-MIST effect that is the subject of this work.

III. PARASITIC-MODE-INDUCED STATE TRANSITIONS: P-MIST

In this section, we analyze how the presence of a parasitic mode ($\mu = 2$) affects the dynamics of a driven fluxonium circuit during a readout pulse. To simulate the linear drive on the readout resonator, we add a drive term $\hat{V}_d = i\xi(\hat{a}_r - \hat{a}_r^\dagger)\cos\omega_d t$ to the system Hamiltonian in Eq. 1. If we consider the fluxonium qubit mode, parasitic modes, and readout resonator, a full numerical analysis of several excitations in the circuit would require a prohibitively large Hilbert space. To truncate our Hilbert space to feasible dimensions for numerical simulations, here we only include a single parasitic mode $\mu = 2$ (as previously justified in Sec. II), and we replace the readout mode with a classical drive term [20, 22, 23] (see derivation in App. C 1). Under this semi-classical approximation, the driven circuit Hamiltonian includes the qubit mode ϕ and the parasitic mode at $\mu = 2$, and is

$$\hat{H}_{s.c.}(\bar{n}_r) = \hat{H}_0 + \hat{V}_{s.c.}(\bar{n}_r). \quad (4)$$

Here, the bare Hamiltonian is

$$H_0 = \hat{H}_\phi + \hat{H}_\mu - \frac{g_{\phi\mu}}{N_{\phi,\mathrm{ZPF}}} \hat{N}_\phi(\hat{a}_\mu - \hat{a}_\mu^\dagger) \quad (5)$$

and the modified drive term $V_{s.c.}$ is

$$\hat{V}_{s.c.}(\bar{n}_r) = \frac{\xi_{\phi r}(\bar{n}_r)}{N_{\phi,\mathrm{ZPF}}} \hat{N}_\phi \cos\omega_d t + \frac{\xi_{\mu r}}{N_{\mu,\mathrm{ZPF}}}(\bar{n}_r)\hat{N}_\mu \cos\omega_d t,$$
$$(6)$$

where the effective drive powers $\xi_{\mu(\phi)r}(\bar{n}_r) = 2g_{\mu(\phi)r}\sqrt{\bar{n}_r}$, and $\bar{n}_r$ denotes the average number of photons in the readout cavity. In the remaining text, we refer to the quantities $\xi_{\phi r/\mu r}$ as "qubit drive strengths" and "parasitic drive strengths", respectively.

Our primary focus is to analyze p-MIST processes that introduce simultaneous transitions in the parasitic mode and the qubit mode. To identify the likely state transitions in the driven circuit, we first examine the energy eigenstates of the bare Hamiltonian $\hat{H}_0$ in Eq. 5. These states will be hybridized fluxonium-parasitic mode states, and we label them as $|\tilde{k}, \tilde{n}\rangle$. A given state $|\tilde{k}, \tilde{n}\rangle$ corresponds to the eigenstate that has the maximum overlap with "bare" fluxonium and parasitic mode states $|k\rangle_\phi \otimes |n\rangle_\mu$, i.e., the eigenstates of H_ϕ and H_μ.

In what follows, we identify relevant state transitions in the driven fluxonium plus parasitic mode system. First, we perform an analysis based on the Floquet eigenstates of our system at a given fixed drive power. Similar to Refs. [21–23] for transmons, we can use this to then simulate the drive ring-up to some chosen final photon number $\bar{n}_r$, and identify potential state transitions. We do this for a range of drive frequencies ω_d. We find that the presence of the parasitic mode $\mu = 2$ significantly increases the number of MIST processes in the system. We analyze the processes that cause these transitions and quantify their rates using perturbative approaches and Landau Zener probability calculations [31]. We also show that the residual population in the parasitic modes, after a readout pulse, can lead to significant dephasing of the reset qubit mode, limiting the performance of the qubit for future use.

A. Recap of the Floquet branch analysis method

Our first numerical analysis involves calculating the Floquet eigenstates of $H_{s.c.}$ (see Eq. 4) for various fixed values of the drive powers, as controlled by the average photon number $\bar{n}_r$. We do this by retaining the lowest 20 levels in the qubit subspace ϕ and 2 levels in the parasitic mode $\mu = 2$[32]; the truncation for this analysis are discussed further in App. C 2. Our goal is to use these results to make predictions for a readout pulse involving a time-dependent drive power, identifying possible transitions starting from a dressed state $|i\rangle = |\tilde{\phi}, \tilde{\mu}\rangle$ where $\phi \in \{0, 1, 2\}$ and $\mu = 0$ (i.e. parasitic mode is initially empty). With $\omega_\mu/2\pi = 12.06$ GHz, the analysis in this section will consider the regime of negative detuning where, $\omega_{\mu=2} > \omega_d = \omega_r \gg \omega_q$, and can be replicated for any other parasitic mode $\mu \neq 2$. Note that we also analyze the effects of an alternative circuit with $\omega_{\mu=2}/2\pi \sim 16$ GHz and $\omega_{01}/2\pi \sim 300$ MHz in Sec. IV.

Inspired by [22, 23], we extract p-MIST processes by tracking the evolution of the Floquet eigenstates as we increase the parameter $\bar{n}_r$, a method known as *branch analysis*. We do this for a series of discrete values of $\bar{n}_r$, that we chose to be integers. The simulation begins in a chosen eigenstate $|i\rangle_0$ of the bare Hamil-
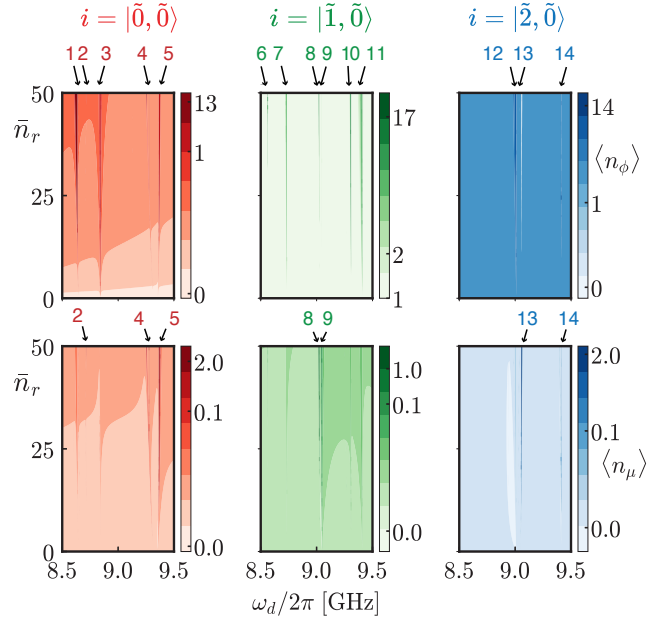

FIG. 3. **MIST and p-MIST processes as seen in Floquet branch simulations.** Each column corresponds to the branch associated with a specific undriven (but dressed) eigenstate $i = |\tilde{k}, \tilde{0}\rangle$. **Top row:** Average fluxonium excitation number in the given branch $\langle n_\phi \rangle$, as a function of drive power ($\propto \bar{n}_r$) and drive frequency ω_d. **Bottom row:** Average excitation number of the $\mu = 2$ parasitic mode, $\langle n_\mu \rangle$. Color scales use a log scaling to help visualize all transitions. Arrows and numbers are used to indicate each transition (with numbers corresponding to Table III). See Figs. 20-22 of App. C 3 b for corresponding behaviour of quasienergies.

tonian $\hat{H}_0 \equiv \hat{H}_{s.c.}[\bar{n} = 0]$ (see Eq. 5). Next, we compute the Floquet eigenstates $|m_1\rangle$ of the Hamiltonian $\hat{H}_{s.c.}[\bar{n}_r = 1]$, corresponding to a single photon increase in the readout resonator. We then identify the Floquet eigenstate of this Hamiltonian $|i\rangle_{\bar{n}_r=1}$ that has maximum overlap with $|i\rangle_{\bar{n}_r=0}$. We repeat this process iteratively, increasing $\bar{n}_r$ by one each time:

$$|i_{\bar{n}_r=k}\rangle : \max_m |\langle i_{\bar{n}_r=k-1}|m_{\bar{n}_r=k}\rangle|^2. \qquad (7)$$

We thus obtain a set of states $|i\rangle_0, |i\rangle_1, |i\rangle_2, ...$ that we refer to as a branch. At a heuristic level, this trajectory of states would describe the adiabatic evolution of the system as the drive power is increased. The drive power in this trajectory is increased to emulate a single photon increase in the readout resonator i.e. $\delta\bar{n}_r = 1$. This corresponds to a constant increase in drive powers (see Eq. 6) $\delta|\xi_{\mu(\phi),r}|^2 = 4g_{\mu(\phi),r}^2$. [SS: We make this choice to emulate the more quantum approach to a branch analysis captured in Ref. [19, 23]. The probability for this ring up is studied further for one of the transitions in Sec. III C. We emphasize that our analysis shows the impact of p-MIST transitions and does not focus on identifying *all* transitions that will be caused due to the N parasitic modes in the fluxonium circuit.]

In Eq. 7, the overlaps between Floquet eigenstates are all computed at a fixed time within each drive period (i.e. at times $t_k = k \times 2\pi/\omega_d$). We have verified

Transition No. (see Fig. 3)	Fluxonium MIST Process	Threshold Drive Photon ($\bar{n}_r$)	Drive Frequency ($\omega_d/2\pi$)	Quasienergy Gap (Δ_{ac})	p-MIST	Drive Photons Absorbed (see Fig. 8)
1.	$|\tilde{0},\tilde{0}\rangle \longleftrightarrow |\tilde{13},\tilde{0}\rangle$	13	8.64 GHz	0.90 MHz	×	3
2.	$|\tilde{0},\tilde{0}\rangle \longleftrightarrow |\tilde{4},\tilde{2}\rangle^*$	48	8.71 GHz	0.06 MHz	✓	4
3.	$|\tilde{0},\tilde{0}\rangle \longleftrightarrow |\tilde{8},\tilde{0}\rangle$	~ 0	8.84 GHz	–	×	2
4.	$|\tilde{0},\tilde{0}\rangle \longleftrightarrow |\tilde{6},\tilde{1}\rangle^*$	46	9.25 GHz	1.63 MHz	✓	2
5.	$|\tilde{0},\tilde{0}\rangle \longleftrightarrow |\tilde{3},\tilde{1}\rangle$	12	9.36 GHz	0.56 MHz	✓	2
6.	$|\tilde{1},\tilde{0}\rangle \longleftrightarrow |\tilde{17},\tilde{0}\rangle$	32	8.56 GHz	0.25 MHz	×	4
7.	$|\tilde{1},\tilde{0}\rangle \longleftrightarrow |\tilde{7},\tilde{0}\rangle$	4	8.73 GHz	0.74 MHz	×	2
8.	$|\tilde{1},\tilde{0}\rangle \longleftrightarrow |\tilde{12},\tilde{1}\rangle$	19	9.02 GHz	0.12 MHz	✓	4
9.	$|\tilde{1},\tilde{0}\rangle \longleftrightarrow |\tilde{2},\tilde{1}\rangle$	11	9.05 GHz	0.66 MHz	✓	2
10.	$|\tilde{1},\tilde{0}\rangle \longleftrightarrow |\tilde{14},\tilde{0}\rangle$	7	9.31 GHz	0.50 MHz	×	3
11.	$|\tilde{1},\tilde{0}\rangle \longleftrightarrow |\tilde{9},\tilde{0}\rangle$	2	9.41 GHz	1.19 MHz	×	2
12.	$|\tilde{2},\tilde{0}\rangle \longleftrightarrow |\tilde{12},\tilde{0}\rangle$	3	9.00 GHz	0.73 MHz	×	2
13.	$|\tilde{2},\tilde{0}\rangle \longleftrightarrow |\tilde{0},\tilde{2}\rangle$	38	9.06 GHz	0.53 MHz	✓	2
14.	$|\tilde{2},\tilde{0}\rangle \longleftrightarrow |\tilde{5},\tilde{1}\rangle^*$	49	9.41 GHz	2.71 MHz	✓	2

TABLE III. Measurement-induced-state-transition (MIST) observed in Fig. 3. Column 1 lists the numbering used to mark the transitions in Fig. 3. Here $|\tilde{i},\tilde{j}\rangle$ indicates the hybridized eigenstate of H_0 (see Eq. 5) which has the maximum overlap with the state $|i\rangle_\phi \otimes |j\rangle_{\mu=2}$ in the disjoint Hilbert space of qubit mode (ϕ) and parasitic mode ($\mu = 2$). Column 2 lists the MIST processes that start at the lowest average readout photon number $\bar{n}_r$ given by column 3. In some cases, we use $\bar{n}_r \sim 0$ to indicate that the drive frequency is exactly resonant with the transition frequency between the two levels. A '*'-marked state indicates hybridization at lower $\bar{n}_r$ due to preceding transitions [a]. Column 4 represents the drive frequency $\omega_d/2\pi$ at which these transitions occur. Column 5 yields the quasienergy gap at the avoided crossing labeled as Δ_{ac}. Column 6 indicates if the process cannot occur without the parasitic mode, denoted as p-MIST. The various colors for the checkmarks indicate that the p-MIST event involves the state $|\tilde{0},\tilde{0}\rangle$ (red), $|\tilde{1},\tilde{0}\rangle$ (green) or $|\tilde{2},\tilde{0}\rangle$ (blue). Column 7 indicates the number of drive photons (#) involved in the energy-conserving process, illustrated in Fig. 8, which is responsible for these transitions.

[a] $|\tilde{4},\tilde{2}\rangle^*$: $|\tilde{4},\tilde{2}\rangle \longleftrightarrow |\tilde{14},\tilde{2}\rangle$ at $\bar{n}_r = 5, \omega_d/2\pi = 8.71$ GHz with $\Delta_{ac} = 4.0$ MHz absorbs 2 drive photons
$|\tilde{6},\tilde{1}\rangle^*$: $|\tilde{6},\tilde{1}\rangle \longleftrightarrow |\tilde{3},\tilde{1}\rangle$ at $\bar{n}_r \sim 0, \omega_d/2\pi = 9.25$ GHz
$|\tilde{5},\tilde{1}\rangle^*$: $|\tilde{5},\tilde{1}\rangle \longleftrightarrow |\tilde{17},\tilde{0}\rangle$ at $\bar{n}_r = 14, \omega_d/2\pi = 9.41$ GHz with $\Delta_{ac} = 4.2$ MHz absorbs 1 drive photon

that our method yields the same results as Ref. [23] (where instead a time-averaged overlap was used). [SS: Thus, we do not see any appreciable difference from not using a time-averaged overlap in Ref. [23] but in less time.]

[SS: We make these choices to observe population change in the fluxonium potential, i.e. state transitions, as we ring up the drive powers. Note that, the slower or more adiabatic the ring-up of the drive, more are the chances to observe a state transition. To avoid fairly weak transitions we ring-up the drive using discrete steps of $\delta\bar{n}_r = 1$ which corresponds to a linear increase in the drive powers. This choice uses a drive strength increment size $\delta|\xi_{\phi(mu),r}| = 2g_{\phi(\mu),r}$, different from the driven transmon analysis in Refs. [23] where $\delta|\xi_{\phi,r}| \sim \kappa_r$, the readout resonator's decay rate. Thus, our simulations can also be used to understand the impact of parasitic state transitions due to a linearly increasing drive on the fluxonium circuit.]

For each state $|i_{\bar{n}_r=k}\rangle$ in a given branch, we compute:

1. The expectation value of the fluxonium excitation-number operator $\hat{n}_\phi = \sum_k k |k\rangle_\phi \langle k|_\phi$, where $|k\rangle_\phi$ is the kth bare fluxonium energy eigenstate,

2. The expectation value of parasitic-mode number operator $\hat{n}_\mu = \hat{a}_\mu^\dagger \hat{a}_\mu$ (for the single mode $\mu = 2$ that we retain), and

3. The quasi-energy of the state $E_i \mod (\omega_d/2\pi)$.

We can thus identify MIST and p-MIST transitions by detecting sudden changes in the number of qubit or parasitic mode excitations as the $\bar{n}_r$ is increased, indicating an unwanted drive-induced hybridization of eigenstates.

B. Branch analysis p-MIST predictions

Fig. 3 illustrates our main result, showing examples of p-MIST drive-induced transitions, for initial states that have maximum overlap with states $|0\rangle_\phi$, $|1\rangle_\phi$ and $|2\rangle_\phi$ in the fluxonium subspace and the ground state $|0\rangle_{\mu=2}$ in the parasitic subspace. For each branch, we use color map to plot the average excitation number of the qubit mode $\langle n_\phi \rangle$ (top row), and the parasitic mode $\langle n_\mu \rangle$, range of readout drive frequencies (horizontal

axes) and final readout cavity average photon numbers $\bar{n}_r$ (vertical axes).

Note that both the drive powers, of the qubit $\xi_{\phi r}$ and of the parasitic mode $\xi_{\mu r}$, are exclusively dependent on $\bar{n}_r$. Thus, we will often interchangeably call $\bar{n}_r$ as the drive power. Results are shown for driven frequencies $\omega_d/2\pi$ in the range $8.5 - 9.5$ GHz [33]; other regimes are discussed in Sec. IV. For one-dimensional slices of the results at fixed $\bar{n}_r$, along with the quasi-energies, see App. C 3 b.

Any streak or sharp change in color intensity represents a sudden and significant jump in the qubit or parasitic mode population, i.e. MIST or p-MIST. The parasitic transitions or p-MIST correspond to simultaneous jumps in the population of the modes ϕ (Figs. 3, top row) and $\mu = 2$ (Figs. 3, bottom row), as $\bar{n}_r$ varies. At these points, an avoided crossing in the quasi-energies of the Floquet states confirms the hybridization of the two states involved in the population exchange (see Figs. 20-22 in App. C 3 b). Additional resonances may occur at alternate drive frequencies not shown in Fig. 3. Table III lists significant transitions observed in our Floquet simulations, and associated processes which cause them, identified through a perturbative analysis (see App. C 3 b) and energy conservation (shown later in Fig. 8). We note that certain MIST processes, including p-MIST, involve transitions at the flux sweet spot [34] between parity-conserving states, due to virtual excitations via non-parity-conserving states.

The above results clearly show that coupling to the JJA parasitic modes enables new MIST processes (beyond what would be predicted by a fluxonium-only simulation). Further, we find that coupling to parasitic modes can alter and even disrupt transitions that would be predicted by a fluxonium-only calculation. For example, consider transition 14 in Table III. For this drive frequency, if one neglects the qubit-parasitic mode coupling, one finds a MIST transition between $|\tilde{2}, \tilde{0}\rangle \leftrightarrow |\tilde{17}, \tilde{0}\rangle$ will occur via the absorption of three drive photons. Including the parasitic mode, the nature of this process changes. As drive power (i.e. $\bar{n}_r$) is increased, one first finds a transition between the states $|\tilde{5}, \tilde{1}\rangle \leftrightarrow |\tilde{17}, \tilde{0}\rangle$ at a threshold drive photon of $\bar{n}_r = 14$. As the drive power is further increased, one obtains at $\bar{n}_r = 41$ a transition $|\tilde{2}, \tilde{0}\rangle \leftrightarrow |\tilde{5}, \tilde{1}\rangle$ (something enabled by the earlier hybridization of $|\tilde{5}, \tilde{1}\rangle$ and $|\tilde{17}, \tilde{0}\rangle$).

Another qualitatively new feature that arises due to the parasitic modes is the possibility of MIST-like transitions where the qubit loses excitations. For example, consider transition 12 in Table III. [SS: In this process, two drive photons are absorbed, the fluxonium state has a downward transition $|2\rangle_\phi \to |0\rangle_\phi$, and the net energy released is used to excite the parasitic mode $|0\rangle_\mu \to |2\rangle_\mu$ By simple energy conservation, such an effect is not possible without a parasitic mode. In fact, this transition can even modify the T_1 lifetime of the $0 - 2$ fluxonium subspace, and not just contribute to leakage like general MIST phenomena.]

[SS: Our results also display branch bunchings (see Figs. 20(2,4) in App. C 3 b for reference) instead of crossings in the negative detuning regime. This is
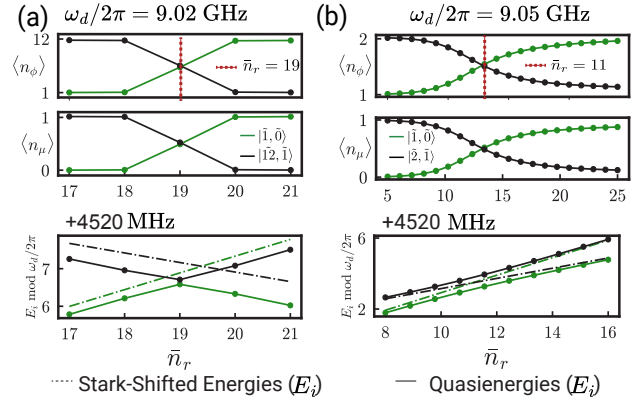

FIG. 4. Examples of p-MIST using transitions **(a)** 8 and **(b)** 9 from Table III involving the $|\tilde{1}, \tilde{0}\rangle$ state, with maximum overlap to the un-hybridized state $|1\rangle_\phi \otimes |0\rangle_{\mu=2}$. **Top row:** Qubit mode average occupation $\langle n_\phi \rangle$. **Middle row:** Parasitic mode average occupation $\langle n_\mu \rangle$. **Bottom row:** Stark-shifted eigen-energies (dashed) from first-order perturbative calculations, and quasi-energies (solid) from Floquet simulations showing avoided crossings. Plots are extracted from numerical data used in Fig. 3. The data points are connected by lines for visual aid.

contrary to Ref. [23] where such branch bunching has been observed only in the positive detuning ($\omega_q > \omega_r$) regime.] Consider for example transitions 3 and 4 in Table III. Here, we are driving at a frequency that exactly matches the transition frequency between two non-computational states, such that these states immediately start to hybridize into an equal superposition of the two original undriven states. For example, in transition 4, the readout drive frequency exactly matches the $|3\rangle_\phi \to |6\rangle_\phi$ transition frequency at zero readout excitations. In this case, levels $|3\rangle_\phi$ and $|6\rangle_\phi$ hybridize for even very small but non-zero drive powers $\bar{n}_r$ (see Fig. 20 in App. C 3 b). [SS: While this effect is not limited to p-MIST, we highlight that the presence of parasitic modes can result into more exotic transitions transitions. For example, in transition 4, one such transition between the states $|\tilde{3}, \tilde{1}\rangle$ and $|\tilde{6}, \tilde{1}\rangle$, where the parasitic mode was excited, eventually lead to a p-MIST effect involving the computational state $|\tilde{0}, \tilde{0}\rangle$. See Fig. 20(4) for explicit population and quasienergy plots involving the three states.]

Our findings reveal that for our specific circuit choice, JJA parasitic modes can become significantly populated, as we show in Fig. 3. Having identified key transitions that cause these effects, we now calculate the transition rates in detail, and the consequence on qubit coherence.

For further insights, we now examine in more detail how quasienergies and excitation numbers change as a function of drive power $\bar{n}_r$ when we pass through an avoided crossing associated with a p-MIST process. Figs. 4(a,b) show explicitly how average qubit and parasitic mode excitation numbers change as a function of drive powers $f(\bar{n}_r)$ for fixed drive frequency corresponding to $8, 9$ in Table III. Both these transitions involve starting in the qubit's first excited state (i.e. branches associated with the undriven state $|\tilde{1}, \tilde{0}\rangle$). The simultaneous exchange of
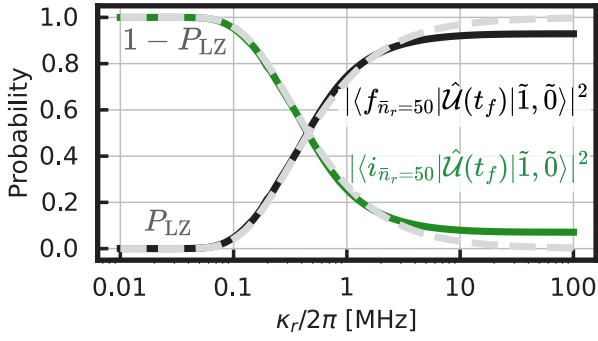
FIG. 5. **p-MIST transition probabilities as a function of readout cavity ring-up rate.** We plot the probabilities for adiabatic (green) and diabatic (black) transitions for a time-dependent ring-up of the average cavity photon number from $\bar{n}_r = 0$ to $\bar{n}_r = 50$, for different choices of the cavity damping rate κ_r which controls the speed of the sweep (see text). We start the system in the qubit's first excited state $|\tilde{1}, \tilde{0}\rangle$. The drive frequency is $\omega_d/2\pi = 9.05$ GHz, corresponding to the crossing shown in in Fig. 4(b). Here, $|f_{\bar{n}_r=50}\rangle$ and $|i_{\bar{n}_r=50}\rangle$ are the final states in the end of branch analyses for $|\tilde{2}, \tilde{1}\rangle$ and $|\tilde{1}, \tilde{0}\rangle$, respectively. The time-evolution operator is denoted by $\hat{\mathcal{U}}(t_f) = \mathcal{T} \exp\left(-i \int_0^{t_f} \hat{H}_{s.c.}(t) dt\right)$ where $\mathcal{T}$ indicates time-ordering and $t_f = 10/\kappa_r$. The adiabatic (green) curve corresponds to an unwanted p-MIST transition. We also plot the predictions of the Floquet branch analysis combined with a Landau Zener approximation for the probabilities (grey), which are in excellent agreement over a wide range of κ_r.

population in the qubit mode ϕ, shown in the top panels, and the parasitic mode $\mu = 2$, shown in the middle panels, confirms that the transitions are indeed p-MIST.

The bottom panel of Fig. 4 shows the corresponding behavior of the branch quasi-energies as a function of drive power, for the same drive parameters. We both plot quasi-energies coming from the Floquet calculations, as well as the predictions of a perturbative calculation including drive-induced Stark shifts (see App. C 3 a for details). For Fig. 4, the perturbative calculations do a good job of showing that there will be a crossing of energies, very near where an avoided crossing is seen in the Floquet calculations; this suggests that a simple picture of the crossings is possible. The Floquet calculations also clearly show an avoided crossing. Note that these transitions occur at relatively modest average readout cavity photon numbers $\bar{n}_r = 11, 19$.

C. Transition probability

Our Floquet branch analysis gives strong evidence that MIST and p-MIST transitions will occur during the ring-up of the resonant during a readout pulse. Here, we validate this approach by focusing on a specific transition, and showing (via explicit time-dependent simulations) that it does indeed occur as predicted. We also show that this full-time-domain simulation is in agreement with a Landau-Zener analysis that takes as inputs the result of the Floquet branch analysis.

We focus on the p-MIST transition shown in Fig. 4(b), which corresponds to a fairly large avoided crossing energy of $\Delta_{ac} = 0.66$ MHz. We will perform a full time-dependent simulation of $\hat{H}_{s.c.}$ in Eq. 4, using time-dependent drive powers that are determined by a time-dependent average readout cavity photon number having the form:

$$\bar{n}_r(t) : \bar{n}_r(1 - e^{-\kappa_r t/2})^2. \tag{8}$$

This corresponds to the ring-up of a resonantly driven cavity with a damping rate κ_r [21–23].

To calculate transition probabilities in this full-time-dependent simulation, we start the system in the dressed state $|\tilde{1}, \tilde{0}\rangle$, evolve under $\hat{H}_{s.c.}(t)$ from a time $t = 0$ to $t = 10/\kappa_r$, and then compute the overlap of this state with the Floquet branches of the two states $|i\rangle = |\tilde{1}, \tilde{0}\rangle$ and $|f\rangle = |\tilde{2}, \tilde{1}\rangle$ associated with our predicted transition. We then repeat this calculation for different choices of κ_r, examining how the transition probabilities vary, with the results shown in Fig. 5. As expected, the probability of remaining adiabatic (green curve) decreases as one increases κ_r. Note here that at large κ_r, adiabatic evolution corresponds to a detrimental p-MIST transition having occurred as the most likely final state $|\tilde{2}, \tilde{1}\rangle$ has an extra qubit and parasitic mode excitation compared to the initial state $|\tilde{1}, \tilde{0}\rangle$.

The above probabilities are in very good agreement with the predictions of our Floquet branch analysis combined with a Landau-Zener approximation to the probability of a non-adiabatic transition (used here in a fashion similar to Ref. [31], see App. C 3 c). These probabilities (P_{LZ}) are shown in grey in Fig. 5. Similar to the transmon case in Ref. [23] we see agreement for most of the values of κ_r between the time-domain simulations and our Landau-Zener calculations using the Floquet quasi-energies. [SS: However, for large $\kappa_r \to \infty$, we observe disagreement on the order of $\sim$ 10%, which we attribute to the complexity of our two-mode system which is very likely to not be explained by the simple picture presented by the Landau Zener physics of a two-level system. It is surprising that despite this complexity we find such good agreement for small κ values.]

D. Post-readout qubit dephasing

The new p-MIST processes we identify here can also potentially create errors *after* the readout pulse is complete, as they lead to a new dephasing channel. A p-MIST process results in a JJA parasitic mode having an excitation after the readout pulse is excited. As there is a non-zero dispersive coupling $\chi_{\mu\phi}$ between these modes and the qubit, and as these modes are believed to have relatively large internal quality factors $\sim 10^4$ [13, 35], this will lead to the qubit acquiring a random phase (tied to the random time at which the parasitic mode relaxes). Below, we show master equation simulation results which quantify the scale of phase errors that would result from such processes.
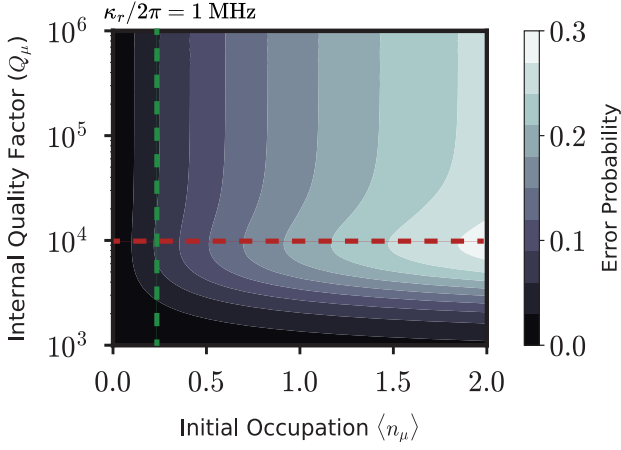
FIG. 6. Dephasing error probability due to random decay of an excited parasitic mode with occupation $\langle n_\mu \rangle$, after p-MIST, for various internal parasitic quality factor Q_μ. The horizontal red line shows the quality factor quoted in [13]. The green line shows the dephasing error probability for transition 9 for various quality factors at $\kappa_r/2\pi = 1$ MHz (see Figs. 4(b) and 5).

For concreteness, we consider a readout pulse with a frequency corresponding to the p-MIST transition labeled 9 in Fig. 4(b)), and for a cavity damping rate $\kappa_r/2\pi = 1$ MHz (which determines the ring-up of the cavity to the maximum drive powers given by $\bar{n}_r = 50$). For these parameters, our previous simulations and Landau-Zener analysis suggest that at the end of the readout pulse, the parasitic mode will have an average non-zero excitation $\langle n_\mu \rangle = 0.25$. In fact, for many transitions this population can be as high as $\langle n_\mu \rangle = 2.0$ as shown in Table III. We now ask how the decay of such population will dephase the fluxonium (assuming it is prepared after readout in the state $|+\rangle = \frac{|0\rangle_\phi + |1\rangle_\phi}{\sqrt{2}}$).

A simple master equation simulation illustrates the resulting qubit dephasing due to this mechanism. We investigate a reduced system of the parasitic mode $\mu = 2$ and the fluxonium qubit (modeled as a two level system), interacting under the dispersive Hamiltonian $\hat{H}_\theta/\hbar = \chi_{\phi\mu} \hat{a}_\mu^\dagger \hat{a}_\mu \sigma_z$, and with a loss dissipator having collapse operator $\sqrt{\kappa_\mu} \hat{a}_\mu$, describing the parasitic mode internal loss. We start the system in a product state, where the parasitic mode has some initial non-zero occupation, and the qubit is in the pure state $|+\rangle$. We let the system evolve for a time $T_f = 10/\kappa_\mu$ long enough to allow the parasitic mode to relax, and then compute the fidelity of the final qubit state with the initial state $|+\rangle$, defining the error probability be the corresponding infidelity. This quantity is plotted in Fig. 6, both as a function of the initial parasitic mode occupancy $\langle n_\mu \rangle$ (given by an incoherent mixture of $|0\rangle_\mu$ and $|2\rangle_\mu$) and its internal quality factor Q_μ. We find that for an internal quality factor Q_μ of 10^4, an initial population of $\langle n_\mu \rangle = 0.25$ in the parasitic mode introduces a dephasing error probability, of about 0.05, which is already past the threshold of the surface code [36]. The explicit time-dependent simulations shown in Fig. 4 indicate that using a realistic readout power of ~ 10 photons, the final post-readout

parasitic mode population is $\langle n_\mu \rangle \sim 0.25$. This population would already be enough to lead to a significant post-readout dephasing effect.

IV. EFFECTS OF CIRCUIT MODIFICATIONS ON P-MIST

The p-MIST processes could actually be mitigated in various ways. Let's explore how adjusting the qubit frequency, readout resonator frequency, and parasitic mode frequencies, could help suppress unwanted transitions. We rely on derivations in Ref. [29] for the circuit in Fig. 2, as well as generalizations introduced in App. A.

A. Coupling Strengths

Fig. 7 identifies the main culprit behind p-MIST as the fluxonium-parasitic-mode coupling, $g_{\phi\mu}$. We compare the results of Floquet branch analyses for the initial state $|\tilde{1}, \tilde{0}\rangle$ under different coupling conditions, drive frequencies, and amplitudes. Fig. 7(a), reproduces the simulation results for our previous coupling strengths $g_{\phi\mu}$ and $g_{\mu r}$ as a reference. In contrast, Fig. 7(b) shows the same simulation but with $g_{\phi\mu}$ set to zero. We observe that a non-negligible $g_{\phi\mu}$ is the main reason for p-MIST effects. This is evident from the absence of parasitic transitions (8, 9) in the top panel, and no streak or sharp change in color indicating parasitic mode excitations in the bottom panel: the parasitic mode population in the absence of this coupling always remains below $\langle n_\mu \rangle = 10^{-4}$.

Further, Fig. 7(c) shows that turning the parasitic-readout coupling to zero shows no reduction in p-MIST. Thus, we can conclude that the qubit-readout coupling $g_{\phi r}$ alone does not cause significant transitions or p-MIST processes without $g_{\phi\mu}$. Turning both parasitic couplings off completely (not shown in Fig. 7) removes any population from the parasitic mode. Therefore, reducing the coupling strength $g_{\phi\mu}$ is a potential path to reducing the likelihood of p-MIST processes.

Next, we analyze the dependence of these coupling strengths on circuit and readout parameters. As discussed, only even-index parasitic modes have a non-zero coupling to the qubit [29] (see derivation in App. A). The coupling strength $g_{\phi\mu}$ between an even parasitic mode and the qubit is given by

$$\frac{g_{\phi\mu}}{2\pi} = \frac{4}{\sqrt{2N}} \frac{\tilde{E}_c^\phi \tilde{E}_{c,\mu}^e c_\mu}{E_{g,j} s_\mu^2} \cdot N_{\phi \mathrm{ZPF}} \cdot N_{\mu \mathrm{ZPF}}, \quad (9)$$

where $c_\mu = \cos \frac{\pi\mu}{2N}$, $\tilde{E}_c^\phi$, $\tilde{E}_{c,\mu}^e$ are the qubit and even parasitic mode charging energies, respectively, and $N_{\phi/\mu,\mathrm{ZPF}}$ are the zero-point fluctuation values for the qubit and parasitic modes. $\tilde{E}_c^\phi$, $N_{\phi/\mu,\mathrm{ZPF}}$ are given in Apps. B 1, and

$$E_{c,\mu}^e = \left[\frac{1}{E_{C_j}} + \frac{1}{4 E_{g,j} s_\mu^2} \right]^{-1}, \quad (10)$$
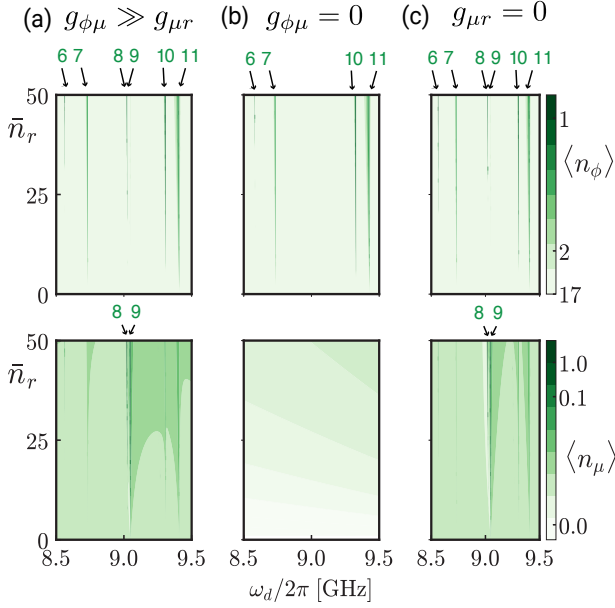
FIG. 7. **Sensitivity of p-MIST processes to parasitic mode coupling strengths.** Panels show the result of Floquet branch analyses for the circuit parameters in Table I. MIST processes observed in Fig. 3 are labeled with numbers and indicated with arrows. **(a)** All parameters the same as Fig. 3(b). **(b)** Same, except now we set the parasitic mode to qubit coupling $g_{\phi\mu}$ to zero. Note that all p-MIST features are now gone. **(c)** Same as (a), but we now set the parasitic mode to readout resonator coupling $g_{\mu r}$ to zero. As with previous Floquet branch analysis plots, color scales use a log scale scale to make transitions more visible.

where $s_\mu = \sin(\frac{\pi\mu}{2N})$. All the other variables represent independent quantities listed in Table I.

By observation, suppressing the parasitic capacitance to ground near the junction array suppresses the qubit-parasitic coupling $g_{\phi\mu}$. However, this is constrained by practical limitations to order $\mathcal{O}(0.1)$ fF per junction. For the parasitic modes with the strongest coupling to the qubit, $\mu \ll N$. The large N, small μ limit with $c_\mu \approx 1$ yields

$$\tilde{E}^e_{c,\mu} \approx 4E_{g,j}s_\mu^2, \quad \tilde{E}^\phi_c \propto \frac{1}{N^2} \implies g_{\phi\mu} \propto \frac{1}{N^{5/2}}. \quad (11)$$

These dependencies are plotted in Fig. 13 of App. B 1. We find that the coupling strength *decreases* with the number of junctions N. Note that changing N changes the target inductance of the qubit. When increasing N, we need to proportionally increase the energies E_{J_j} to fix the inductive energy of the qubit ($E_L = E_{J_j}/N$). However, E_{J_j} is constrained within a typical fabrication process window, capping the maximum E_L. This further supports the large N approximation $\tilde{E}^e_{c,\mu} \approx 4E_{g,j}s_\mu^2$ (see Eq. 10). Thus, the number of junctions N can be optimized to decrease $g_{\phi\mu}$ while keeping E_L constant.

Note that, increasing N while keeping $E_L, E_{g,j}$ constant decreases the parasitic charging energy (see Fig. 13 in App. B 1). For large N and small μ limit,

$$\tilde{E}^e_{c,\mu} \propto 1/N^2, \quad (12)$$

which corresponds to lowering the parasitic mode frequency ω_μ with increasing N. This outcome is generally not favorable towards reducing p-MIST, as discussed in the next section. However, in the absence of any coupling to the qubit $g_{\phi\mu}$, even a low frequency parasitic mode will be of no consequence to p-MIST effects. [AC: End of Aash edits Oct. 22]

B. Mode Frequencies

An alternate strategy is to tailor the circuit so that the resonance conditions required for p-MIST are never realized. We can estimate these conditions by identifying energy-conserving processes, where x drive photons are converted into a transition with an energy difference $\tilde{\Delta}_{if,y}$ in the hybridized eigenspace of the fluxonium and parasitic mode $\mu = 2$. Here, $\tilde{\Delta}_{if,y}$ is the transition energy between levels $|\tilde{i}, \tilde{m}\rangle$ and $|\tilde{f}, \tilde{n}\rangle$ such that $|m - n| = y$. This equation can also be interpreted as a process where x readout photons convert into y parasitic mode photons and a fluxonium excitation $|i\rangle_\phi \leftrightarrow |f\rangle_\phi$ such that $\Delta_{if} = \hbar|\omega_f - \omega_i|$. To guide intuition for understanding the spectrum of resonance conditions, we plot such energy-conserving processes in Fig. 8, for the lowest-order case of $\mu = 2$, that satisfies $|x\omega_r - \tilde{\Delta}_{if,y}/\hbar| \le \epsilon$ which, in the disjoint Hilbert space corresponds to,

$$|x\omega_r - y\omega_\mu - \Delta_{if}/\hbar| \le \epsilon. \quad (13)$$

Here, the buffer $\epsilon/2\pi = 25$ MHz is allowed in this energy conservation to accommodate approximate values for Stark shifted eigen-energies under the readout drive (see App. C 3 a for details).

The energy profile in Fig. 8 shows all four-photon processes allowed in the target drive frequency regime when starting in one of the four lowest fluxonium levels involved in the readout. The results from Floquet simulations are shown in solid dots and labeled in black (see Sec. III), while the processes not identified in the simulation are faded. Note that there are downward transitions from $|2\rangle_\phi$ (blue dots) to the states $|1\rangle_\phi$ (green line) and $|0\rangle_\phi$ (red line) in the fluxonium subspace in the presence of parasitic modes. An example is captured by transition 14 of Table I.

The parenthesized labels in color denote the number of readout photons (xr) and parasitic mode photons (yp) required for the transition in the fluxonium subspace, where a positive index denotes absorption/de-excitation while a negative index denotes emission/excitation. For example, transition 2 corresponds to the emission of four readout photons, which are converted into two parasitic mode photons, absorbed by the mode $\mu = 2$, as well as an excitation from $|0\rangle_\phi$ to $|4\rangle_\phi$ in the fluxonium subspace.

Intuitively, many readout photons are required to bridge a large gap between the readout frequency and parasitic mode frequency. As the gap increases, the likelihood of p-MIST processes decrease. We verify this intuition for different ranges of the various mode frequencies in the following discussion.
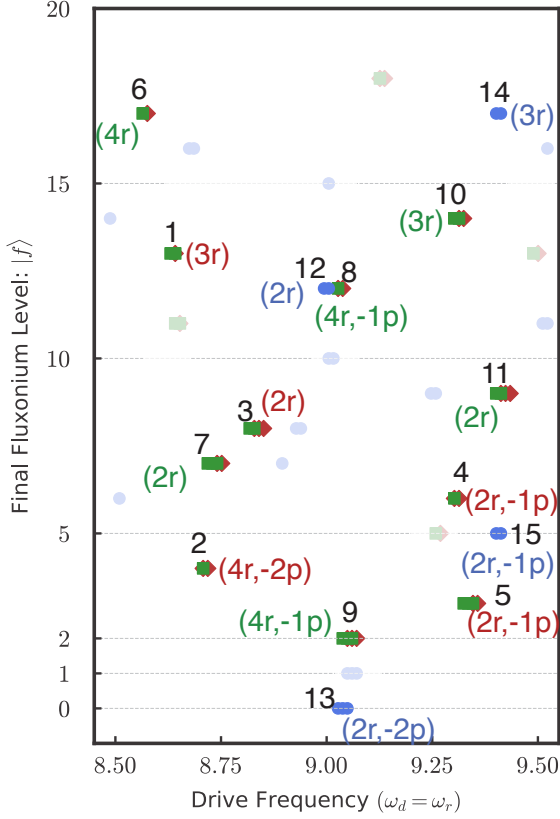
FIG. 8. Energy conserving processes $|\tilde{i}, \tilde{0}\rangle \leftrightarrow |\tilde{f}, \tilde{y}\rangle$ for Eq. 13 with $x \leq 4, y \leq 2, f \leq 20$ and $i = 0$ (red diamonds), $i = 1$ (green squares), $i = 2$ (blue circles). The horizontal lines indicate the initial state i for visual aid. Labels in black correspond to transition # listed in Table III. The colored labels correspond to the disjoint subspaces for simplified representation but the energy conservation uses the eigen-energies of the hybridized eigenstates of H_0 (see Eq. 5). For example, the green label $(4r, -1p)$, for transition 8 of Table III, shows the number of readout photons absorbed (4) and the number of parasitic mode ($\mu = 2$) photons emitted (1) in the process. The faded points are weaker transitions not captured in the Floquet simulations.

a. *Drive Frequency (ω_d):* If $\omega_d \gg \omega_{\mu=N-1}$, a dominating transition mechanism for p-MIST would correspond to an excitation of a strongly coupled, low-frequency parasitic mode (i.e., $\mu = \{2, 4, 6\}$) to a large photon number y, leaving just enough energy to produce excitation to some state f in the fluxonium subspace of significant charge matrix elements (see Fig. 14). However such large excitations in the parasitic modes would occur with lower probability, because of the high photon number y involved in the transition. A full study of this case requires a large Hilbert space and is beyond the scope of this work.

For low-frequency readout ($\omega_d \ll \omega_{\mu=2}$), on the other hand, a large readout photon number x would be needed while having a similar impact. We give the Floquet figure corresponding to a low-frequency readout in Fig. 9 which shows higher parasitic mode populations compared to our previous case in Fig. 3. The p-MIST effects can be explained by examining the increased density of resonances when $\omega_d/2\pi \approx 6$ GHz.
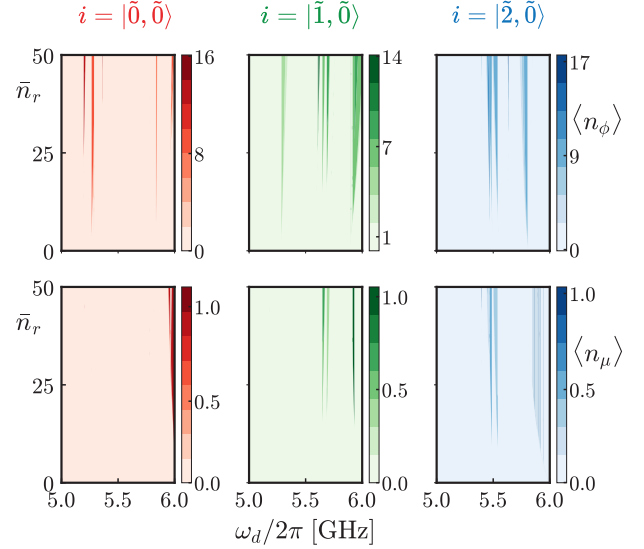

FIG. 9. Floquet simulations at lower readout frequencies using circuit parameters quoted in Tables I and II for branch analysis starting in the dressed hybridized eigenstate $i = |\check{k}, \tilde{0}\rangle$, with maximum overlap to the unhybridized states $|k\rangle_\phi \otimes |0\rangle_{\mu=2}$. The figures are plotted in linear scale, unlike Fig. 3, making any streak due to significantly weaker transitions unnoticeable.

Note that this frequency is approximately the fluxonium plasma frequency $\omega_{12}/2\pi$ and is also half the parasitic mode $\mu = 2$ frequency. This introduces multiple frequency collisions, which cause the various transitions observed in the figure. This logic already indicates that $5.5 - 6$ GHz would be a bad range of frequencies for the current choice of parameters. Formal transition probability calculations, same as Sec. III C, will be required to predict the how detrimental these effects can be. However, the energy conservation indicates that in spite of the increase in the number of p-MIST effects, such transitions will be higher-order processes (large x) which will not take place unless $\bar{n}_r$ is extremely large.

Further lower ω_d for readout is not favorable due to thermal heating of the readout resonator leading to photon-shot-noise induced dephasing of the qubit, and hence not analyzed in this work.

b. *Parasitic Mode Frequency:* Another approach towards mitigating p-MIST processes is to adjust ω_μ so that $\omega_\mu \gg \omega_r$ for $\mu = 2$, requiring more readout photons to be absorbed in p-MIST processes and therefore reducing p-MIST transition rates. The dependence of the parasitic mode frequencies for even μ is

$$\frac{\omega_\mu^e}{2\pi} = \sqrt{8 E_{c,\mu}^e E_{J_j}} \qquad (14)$$

See Eq. 10 for $E_{c,\mu}^e$ and Table I for E_{J_j}. Again, we focus on large N and small μ limit to focus on parasitic modes with the strongest coupling to the qubit. Eqs. 11-12 show that, for large N and small μ limit, ω_μ^e is inversely proportional to N^2 and $C_{g,j}$ [fF] $= \frac{19.4}{E_{g,j} \text{ [GHz]}}$ (see Fig. 13 in App. B 1). Thus, again, a smaller parasitic ground capacitance $C_{g,j}$ increases the parasitic mode charging energy, thus increasing
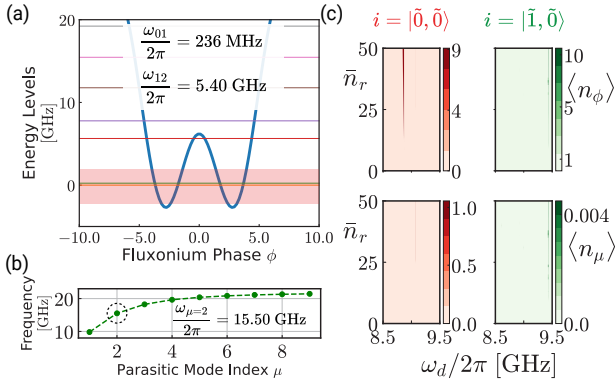
FIG. 10. Floquet analysis with alternate JJA fluxonium parameters inspired by Ref. [6]. **(a)** Fluxonium energy spectrum. **(b)** Parasitic mode frequencies. **(c)** Floquet simulations for the branch analysis of the computational states. Circuit parameters for this circuit are discussed in Sec. IV C and App. D. The Floquet figures are plotted in linear scale unlike Fig. 3, making any streak due to significantly weaker transitions unnoticeable.

its frequency, favorably. However, in contrast with the case of coupling strength $g_{\phi\mu}$, a larger N leads to lower frequencies for these modes, which is unfavorable since it decreases the gap between the between ω_d and ω_μ. We already discussed the complications of changing the ground capacitance $C_{g,j}$ in Sec. IV A. The impact of decreasing N would require consideration of nonlinear corrections as well as fixed inductance, thus, again making these changes difficult in practice [29].

C. Alternative Circuit Parameters

In the previous sections, we considered a fluxonium qubit frequency of ~ 30 MHz. To extend our results to other experiments, we consider these circuit in Fig. 2(a) with a different set of parameters inspired by Ref. [6] and show p-MIST processes in with a fluxonium qubit frequency of $\omega_{01}/2\pi \sim 300$ MHz (see App. D for circuit parameters). The parasitic mode frequency of the $\mu = 2$ mode is $\omega_{\mu=2}/2\pi = 15.50$ GHz. The coupling strengths are: $g_{\phi r}/2\pi = 37$ MHz, $g_{\phi\mu}/2\pi = 216$ MHz, $g_{\mu r}/2\pi = 6$ MHz. The plasma frequency is $\omega_{12}/2\pi = 5.40$ GHz. Importantly, here we only plot results for $|\tilde{0}, \tilde{0}\rangle$ and $|\tilde{1}, \tilde{0}\rangle$ because given Ref. [6] uses only the first two levels for readout as well as computation. The assumptions for numerical modeling are the same as previous Floquet simulations as discussed in App. C 2. Even though the coupling strengths for these circuit parameters are similar to Table II, since $\mu = 2$ is larger by about 4 GHz, we expect fewer p-MIST processes for the drive frequency range analyzed in Fig. 3.

Fig. 10 shows that indeed, p-MIST effects are comparatively less likely for this alternate circuit. The single p-MIST process observed in the Floquet profile $|\tilde{0}, \tilde{0}\rangle \leftrightarrow |\tilde{4}, \tilde{1}\rangle$ occurs at $\bar{n}_r = 25$ and has the quasi-energy gap of $\Delta_{ac} = 0.13$ MHz at the avoided crossing. The quasienergy gap at the avoided cross-

ing for this transition is $\Delta_{ac} = 0.12$ MHz. The corresponding Landau-Zener probabilities and explicit transitions with quasienergies for the Floquet profile in Fig. 10 can be found in App. D. However, a detailed understanding of this Floquet profile, including rate calculations, is necessary to make proper claims about the target drive frequency regime inducing a favorably reduced number of MIST processes, and is left as future direction.

V. CONCLUSION AND FURTHER WORK

In this work, we have analyzed the impact of parasitic modes on driven JJA fluxonium qubits, showing that measurement-induced state transitions of a fluxonium qubit can occur via excitations of a parasitic mode of the JJA. These transitions occur at particular resonance conditions when the energy of several readout photons is equal to a small number of parasitic mode excitations and a fluxonium mode excitation. We refer to these transitions as parasitic-mode-induced-state-transitions or p-MIST, inspired by the term MIST for measurement-induced-state transitions [24]. We find that p-MIST transitions occur at considerable rates because of the strong coupling between the parasitic mode and qubit mode. Consequently, one may expect qubit state transitions via the JJA mode in fluxonium during readout, even at low average readout photon numbers and within the typical requirements for high fidelity, dispersive readout. We show that p-MIST does lower the onset of MIST processes to ~ 10 readout photons at certain drive frequencies. In addition, it has the potential to significantly dephase the qubit, which could in turn limit the qubit gate fidelities required for quantum error correction, and ultimately the performance of a quantum processor. However, the coupling is still sufficiently weak such that, for the vast majority of readout frequencies, p-MIST processes are off-resonant and the JJA mode excitation population is negligible. Therefore, an architect of the quantum circuit may avoid p-MIST with a judicious choice of readout, junction array, and fluxonium parameters.

We observed p-MIST transitions despite imposing various symmetries which should suppress them. In particular, the parallel circuit considered in this work utilizes a specific symmetry, which removes the coupling between parity-odd modes and the qubit. We have shown that this symmetry is preserved even if the readout resonator is coupled to a floating or grounded fluxonium at a single point. Additionally, our analysis only considers fluxonium with external flux of one-half flux quantum. This introduces additional symmetries, forbidding transitions between parity-conserving states via first-order transitions, and even further restricting the possible transition pathways of p-MIST.

We analyze the trend in p-MIST for various drive frequencies, parasitic mode frequencies, coupling constants, and circuits with two different qubit frequencies equal to ~ 30 and ~ 300 MHz. The assumptions we make are crucial to our MIST analysis. Increasing N can reduce the nonlinearity of the para-

sitic modes, with results provided in Sec. IV. We also neglect the self-nonlinearity of the readout mode, following common practice in recent MIST-related analysis [19, 22, 23]. While the effects of nonlinearity in parasitic and readout modes may have a significant impact on the readout fidelity, and perhaps even introduce additional p-MIST transitions, Floquet simulations including the self-nonlinearity of these modes are beyond the scope of our work. Finally, we treat all junctions in the array as identical. However, in practice, the capacitance to ground along the junction array will have some variation, potentially changing the JJA mode structure.

To further study the implications for practical implementation, we suggest adding noise to the Floquet framework [37] and extending our results to include readout fidelity values, using input-output theory. Future work should also incorporate the intrinsic nonlinearity of both the junction array modes and the readout mode. Mitigating parasitic mode excitations could involve careful selection of the readout resonator frequenyc, and varying junction energies along the array to localize parasitic modes, thereby altering the parasitic mode spectrum and reducing excitation probability. Alternative readout schemes like longitudinal readout or cloaking could also be explored with renewed motivation [38–40].

Finally, given the strong coupling between parasitic modes and fluxonium, these modes could even be used as the readout resonator for the fluxonium qubit. In this case, a Purcell filter would be needed to protect the qubit from radiative decay, while coupling the $\mu = 2$ parasitic mode to the Purcell filter and readout feed-line. This approach could help to alleviate the stringent capacitive loading constraints that plague the high-impedance fluxonium qubit.

We have presented a first analysis toward understanding the role of parasitic modes in the readout dynamics of a fluxonium circuit. The circuit parameters used in this work correspond to a parasitic mode of the fluxonium's junction array. However, other modes with similar frequencies may also participate in the environment of the fluxonium. This may include, for example, confined package modes, slot line modes, and harmonics of coplanar waveguide resonators for readout. Our results show the significance of including all modes involved in a circuit when driving many excitations into highly nonlinear circuits.

VI. ACKNOWLEDGMENTS

Parameters	Variables	Values
Phase-slip JJ capacitance	C_p	13.3 fF
Differential capacitance	C	1.14 fF
JJA capacitance energy	C_j	26.2 fF
JJA ground capacitance	$C_{g,j}$	0.1 fF
Phase-slip ground capacitance	$C_{g,p}$	10 fF
Coupling capacitance	C_c	1 fF
ZPF of the resonator/drive	V_{ZPF}	0.75 GHz
ZPF of fluxonium charge operator	$N_{\phi,\mathrm{ZPF}}$	0.36
ZPF of parasitic charge operator	$N_{\mu=2,\mathrm{ZPF}}$	1.58

TABLE IV. Capacitances and zero-point fluctuation (ZPF) values for the fluxonium readout circuit used in the main text.

Appendix A: Single-Point Connections

The fluxonium readout circuit shown in Fig. 2 of main text cn have several modifications, each of which may affect various performance metrics. Here, in Fig. 11, we present two modifications to the parallel circuit, with different grounding options for the fluxonium while the readout resonator is grounded. We will refer to these circuit choices as: H_1, parallel circuit in Fig. 11(a) (same as Fig. 2), H_2, floating fluxonium circuit in Fig. 11(b), and H_3, grounded fluxonium circuit in Fig. 11(c). We adjust the coupling capacitances (using $C_c' = 5.06$ fF, C_c" $= 4.12$ fF in Figs. 11(b,c)) and the total capacitance of the phase slip junction (busing $C' = 4.97$ fF, C" $= 5.8$ fF in Fig. 11(b,c)), as compared to the values for the parallel circuit given by Table IV. These modifications achieve the same qubit frequency $\omega_{01}/2\pi$, plasmon frequency $\omega_{12}/2\pi$, qubit-readout coupling constant $g_{\phi\mu}$ and qubit-readout dispersive shift $\chi_{\phi r}$ for the three circuits as given by Table II. Under these choices, we find that the readout parameters affected by parasitic modes are roughly the same across all three circuits, given our assumptions of ordered array and no self-nonlinearity in parasitic modes. See Table V in App. B for details.

We will now derive the Hamiltonians for the circuits in Figs. 11(b,c) to be used in the next section for comparison. To do this, we follow the recipe given in Ref. [29] for the parallel circuit shown in Fig. 11(a) or Fig. 2(a). Importantly, we will show that the symmetry in the parallel circuit which prevents any coupling with the lowest-frequency parasitic mode ($\mu = 1$) is preserved in all three circuits, absence of which would have changed the Floquet landscape acorss the three circuits significantly.

1. Floating Fluxonium Circuit

The Lagrangian corresponding to these circuits is a combination of the Lagrangians $\mathcal{L}_g$ from the phase-slip junction (comprising of the junction with $E_J/E_C \sim 5 - 8$ and the capacitor C), $\mathcal{L}_g$ from the ground ca-
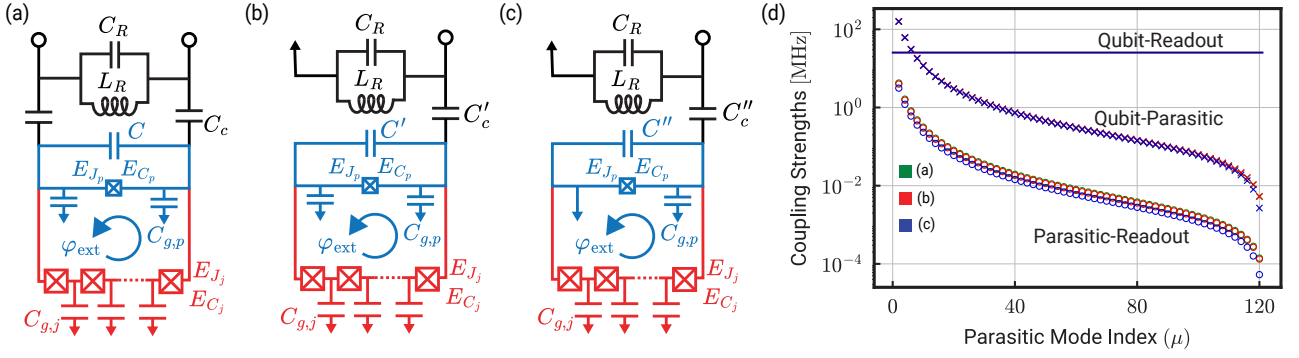
FIG. 11. (a-c) Alternative readout circuits. (a) Parallel circuit (H_1), (b) Floating fluxonium (H_2), (c) Grounded fluxonium (H_3). Alternatives (b) and (c) require a single-point connection to the readout line V, unlike the parallel circuit in (a). We maintain the values for all circuit variables the same as used for the case of the parallel circuit in Fig. 2. (d) Absolute values of the coefficients of coupling terms in the Hamiltonian (in GHz). We can see that the parasitic modes couple to the qubit stronger than the qubit couples to the readout. The parasitic mode coupling to the readout is very slightly weaker in H_3 compared to H_1, H_2. Need to add the flux variables in Figs.(a,b,c)

pacitances, $\mathcal{L}_R$ from the readout resonator and $\mathcal{L}_c$ due to the coupling capacitances C_c and the external voltage V. We mark the flux points across JJA using φ_0 and φ_N in Figs. 11(b,c). We start with an inhomogenous junction array and will use the assumption of ordered junction later in the derivation. The flux variables and voltage variables in the circuit are denoted by $\varphi_n = 2\pi\Phi_n/\Phi_0$ and $\dot{\varphi}_n = 2\pi V_n/\Phi_0$, respectively, where $\Phi_0 = h/2e$ is the superconducting flux quantum. We will use subscripts j, p for JJA and the phase-slip junction coordinates, respectively. Transforming the Lagrangian in Ref. [29], the following terms will remain the same in the case of floating fluxonium circuit:

$$\mathcal{L} = \mathcal{L}_{phase-slip} + \mathcal{L}_{JJA} + \mathcal{L}_g + \mathcal{L}_R + \mathcal{L}_C \tag{A1}$$

$$\mathcal{L}_{phase-slip} = \frac{(\dot{\varphi}_N - \dot{\varphi}_0)^2}{16E_{C'}} - E_{J_p}\cos(\varphi_0 - \varphi_N + \varphi_{ext}) \tag{A2}$$

$$\mathcal{L}_{JJA} = \sum_{n=1}^{N} \frac{(\dot{\varphi}_n - \dot{\varphi}_{n-1})^2}{16E_{C_j}^n} - E_{J_j}^n\cos(\varphi_n - \varphi_{n-1}) \tag{A3}$$

$$\mathcal{L}_R = \frac{\dot{\varphi}_-^2}{16E_R} - \frac{\varphi_-^2}{16E_R} \tag{A4}$$

$$\mathcal{L}_g = \sum_{i=0}^{N} \frac{\dot{\varphi}_n{}^2}{16E_{g_i}} \tag{A5}$$

The change in this Lagrangian is primarily due to the fewer coupling capacitances such that,

$$\mathcal{L}_c = \frac{(\dot{\varphi}_{-1} - \dot{\varphi}_0)^2}{16E_{c'}} = \frac{\dot{\varphi}_0^2}{16E_{c'}} + \frac{\dot{\varphi}_{-1}^2}{16E_{c'}} - \frac{\dot{\varphi}_0\dot{\varphi}_{-1}}{8E_{c'}} \tag{A6}$$

Now, we define the guage-invariant phase difference quadratures

$$\varphi_m - \varphi_0 = \sum_{l=1}^{m} \theta_l \tag{A7}$$

and use the fluxoid quantization with an external flux $\varphi_{ext} = \pi$.

$$\tag{A8}$$

$$\sum_{m=0}^{N} \theta_m + \varphi_{ext} = 2\pi z, \tag{A9}$$

where $z \in \mathbb{Z}$ is an arbitrary integer. Writing the lagrangian in this new basis yields the expression,

$$\dot{\varphi}_0 = E_t\left(\frac{\dot{\varphi}_{-1}}{E_{c'}} - \sum_{n=1}^{N}\sum_{m=n}^{N} \frac{\dot{\theta}_n}{E_{g_m}}\right) \tag{A10}$$

where

$$E_t = \left(\frac{1}{E_{c'}} + \sum_{n=0}^{N} \frac{1}{E_{g_n}}\right)^{-1} \tag{A11}$$

is the total capacitive energy of the circuit due to the parasitic and coupling capacitances.

$$\therefore \mathcal{L}_g + \mathcal{L}_c = \frac{\dot{\varphi}_{-1}^2}{16E_{c'}}\left(1 - \frac{E_t}{E_{c'}}\right) + \sum_{n=1}^{N} \frac{\dot{\varphi}_{-1}\dot{\theta}_n}{E_{c'}}\left(\sum_{i=n}^{N} \frac{E_t}{8E_{g_i}}\right)$$
$$+ \sum_{m=1}^{N}\sum_{n=1}^{N} \dot{\theta}_m\dot{\theta}_n\left(\sum_{j=\max\{m,n\}}^{N} \frac{1}{16E_{g_j}}\right)$$
$$\times \left(1 - \sum_{i=\min\{m,n\}}^{N} \frac{E_t}{E_g^i}\right) \tag{A12}$$

We simplify the Lagrangian $\mathcal{L}_g + \mathcal{L}_c$ as

$$= \frac{\dot{\varphi}_{-1}eV}{8E_c} + \frac{\dot{\varphi}_{-1}^2}{16}\left(\frac{1}{E_c}\left(1 - \frac{E_t}{E_c}\right) + \frac{1}{E_c}\right)$$
$$+ \sum_{n=1}^{N}\left(\frac{\dot{\varphi}_{-1}\dot{\theta}_n}{E_c}\right)(N - n + 1)\frac{E_t}{8E_g} + \frac{(\dot{\varphi}_{-2})^2}{16E_c^4}$$
$$+ \sum_{m=1}^{N}\sum_{n=1}^{N} \dot{\theta}_m\dot{\theta}_n \frac{(N - \max\{m,n\} + 1)\min\{m,n\}E_t}{16E_g^2} \tag{A13}$$

a. Assumptions. The first line show that the contribution from the coupling capacitance comes only via the readout resonator mode. The second and third lines, on the other hand, show the terms which contribute to parasitic couplings via the the ground capacitance due to terms proportional to $\dot{\theta}_m \dot{\theta}_n$. Now, we will assume an ordered array such that

$$
\begin{aligned}
C_{g_1} &= ...C_{g_{N-1}} = C_{g,j} \\
C_{g_0} &= C_{g_N} = C_{g,p} \\
E_{J_1} &= ... = E_{J_N} = E_{J,j} \\
C_{j_1} &= ... = C_{j_N} = C_j
\end{aligned}
$$

b. Collective Modes. Now, we will define the collective modes for the fluxonium circuit, $\{\phi, \xi_1, ..., \xi_{N-1}\}$ such that

$$
\theta_m = \phi/N + \sum_\mu W_{\mu m}\xi_\mu, \tag{A14}
$$

and inversely,

$$
\phi = \sum_m \theta_m, \quad \xi_\mu = \sum_m W_{\mu m}\theta_m. \tag{A15}
$$

Here, ϕ is called the superinductance mode or the *qubit* mode while ξ_μ denote the parasitic modes indexed by $\mu \in \{1, .., N-1\}$ [28]. The matrix W is semi-orthogonal, with dimensions $(N-1) \times N$, and is given by $\sum_m W_{\mu m}W_{\nu m} = \delta_{\mu\nu}$. Its row sum is zero, $\sum_m W_{\mu m} = 0$. Thus, the following choice

$$
W_{\mu m} = \sqrt{\frac{2}{N}} \cos \frac{\pi\mu(m-1/2)}{N}, \tag{A16}
$$

is observed in [28] and later used in [29] to derive the Hamiltonian for the parallel circuit. The choice of these new variables highlights the collective modes describing the low-energy physics as illustrated in [26, 41, 42]. We can now split the combined Lagrangian $\mathcal{L} = \mathcal{T} - \mathcal{U}$ into kinteic energy $\mathcal{T}$ and potential energy $\mathcal{U}$ terms in the basis of collective modes as, [SS: Here on, we need to remove terms due to Ec3 and Ec4, and also point out where the symmetry from the odd modes is coming from. We also need to separate Egj and Egp]

$$
\begin{aligned}
\mathcal{T} =& \frac{\dot{\varphi}_{-1}^2}{16E_{c'}}\left(1 - \frac{E_t}{E_{c'}}\right) + \frac{1}{E_{c'}}\left(1 - \frac{E_t}{E_{c'}}\right) \\
&+ \Big[\sum_{n=1}^{N}\left(\frac{\dot{\varphi}_{-1}}{E_c} + \frac{\dot{\varphi}_{-2}}{E_c}\right)\left(\frac{E_t}{8E_c} + (N-n+1)\frac{E_t}{8E_g}\right) \\
&- \sum_{n=1}^{N}\frac{\dot{\varphi}_{-2}}{8E_c}\Big](\dot{\phi}/N + \sum_\mu W_{\mu n}\dot{\xi}_\mu) + \sum_{m=1}^{N}\sum_{n=1}^{N}(\dot{\phi}/N \\
&+ \sum_\mu W_{\mu n}\dot{\xi}_\mu)(\dot{\phi}/N + \sum_\mu W_{\mu m}\dot{\xi}_\mu)\Big((N - \max\{m,n\} \\
&+ 1)\frac{1}{16E_g} + \frac{1}{16E_c}\Big)\left(\min\{m,n\}\frac{E_t}{E_g} + \frac{E_t}{E_c}\right)
\end{aligned}
\tag{A17}
$$

$$
\mathcal{U} = -E_{J_p}\cos(\phi) - \frac{(\varphi_{-1} - \varphi_{-2})^2}{16E_R} \\
- \sum_{n=1}^{N} E_{J_j}\cos\left(\phi/N + \sum_\mu W_{\mu n}\xi_\mu\right) \tag{A18}
$$

c. Symmetries in the Lagrangian Simplifying the kinetic energy term from Eq. A17, recalling that $\sum_m W_{\mu m} = 0$, and the semi-orthogonal matrix condition $\sum_m W_{\mu m}W_{\nu m} = \delta_{\mu\nu}$ yields

$$
\begin{aligned}
\mathcal{T} =& -\frac{\dot{\varphi}_{-2}eV}{16E_{c'}} + \frac{\dot{\varphi}_{-1}eV}{16E_{c'}} - E_t\frac{\dot{\varphi}_{-1}\dot{\varphi}_{-2}}{16E_{c'}^2} \\
&+ \frac{\dot{\varphi}_{-1}^2}{16}\left(\frac{1}{E_c}\left(1 - \frac{E_t}{E_c}\right) + \frac{1}{E_c}\right) \\
&+ \frac{\dot{\varphi}_{-2}^2}{16}\left(\frac{1}{E_c} + \frac{1}{E_c}\left(1 - \frac{E_t}{E_c}\right)\right) \\
&+ \frac{E_t}{8E_c^2}\dot{\varphi}_{-1}\dot{\phi} + \frac{E_t}{8E_c^2}\dot{\varphi}_{-2}\dot{\phi} \\
&+ \Big[\sum_{n=1}^{N}\left(\frac{\dot{\varphi}_{-1}}{E_c} + \frac{\dot{\varphi}_{-2}}{E_c}\right)\left(\frac{E_t}{8E_c} + (N-n+1)\frac{E_t}{8E_g}\right) \\
&- \sum_{n=1}^{N}\frac{\dot{\varphi}_{-2}}{8E_c}\Big](\dot{\phi}/N + \sum_\mu W_{\mu n}\dot{\xi}_\mu) \\
&+ \Big[(M_{00} + G_{00})\dot{\phi}^2 + 2\sum_\mu(M_{0\mu} + G_{0\mu})\dot{\phi}\dot{\xi}_\mu \\
&+ \sum_{\mu,\nu}(M_{\mu\nu} + G_{\mu\nu})\dot{\xi}_\mu\dot{\xi}_\nu\Big],
\end{aligned}
\tag{A20}
$$

where the coefficients are given by

$$
M_{00} = \frac{1}{16E_{C'}} + \frac{1}{16NE_{C_j}}, \quad M_{0\mu} = 0, \quad M_{\mu\nu} = \frac{\delta_{\mu\nu}}{16E_{C_j}} \tag{A21}
$$

$$
G_{00} = \frac{1}{64E_t}\left(1 - \frac{E_t}{E_c}\right)^2\left[1 - \frac{2}{3}\frac{N-1}{N}\right] \tag{A22}
$$

$$
G_{0\mu} = -\frac{c_\mu o_{\mu+1}}{16E_g\sqrt{2N}s_\mu^2}\left(1 - \frac{E_t}{E_c}\right) \tag{A23}
$$

$$
G_{\mu\nu} = \frac{1}{64E_g s_\mu^2}\left[\delta_{\mu\nu} - \frac{E_t}{E_g}\frac{2c_\mu c_\nu o_\mu o_\nu}{N s_\nu^2}\right]. \tag{A24}
$$

[SS: Define c,o.] The quantities $G_{00}, G_{0\mu}, G_{\mu\nu}$ contribute to the equations for coupling strengths while $M_{00}, M_{\nu\nu}$ contribute to the charging energies of the qubit and parasitic modes, discussed in Sec. IV. Note that G_{00} increases quadratically with a factor of $\left(1 - \frac{E_t}{E_c}\right)$. Thus, $G_{0\mu}$ is different from the parallel circuit by a factor $\left(1 - \frac{E_t}{E_c}\right)$. The last term, $G_{\mu\nu}$ same as the case of parallel circuit quoted in Ref. [29] because it has no dependence on coupling capacitances.

d. Linear Approximation From here on, we define a sum over m, n as running from 1 to N, while the sum over μ, ν runs from 1 to $N-1$. Simplification to including only linear terms from Taylor expansion of the cosine ($\cos x \sim 1 - \frac{x^2}{2}$) Eq. A18 and using $\sum_n W_{\mu m}W_{\nu m} = \delta_{\mu\nu}$, yields (up to a constant term)

$$
\begin{aligned}
\mathcal{U} =& E_{J_p}\cos(\phi) - \frac{(\varphi_{-1} - \varphi_{-2})^2}{16E_R} \\
&+ \frac{E_{J_j}}{2N}\phi^2 + \frac{E_{J_j}}{2}\sum_\mu \xi_\mu^2
\end{aligned}
\tag{A25}
$$

$$
= E_{J_p}\cos(\phi) + \frac{E_{J_j}}{2N}\phi^2 + \frac{E_{J_j}}{2}\sum_\mu \xi_\mu^2 - \frac{\varphi_-^2}{16E_R}, \tag{A26}
$$

where $\dot{\phi}_{-1} = -\dot{\phi}_{-2} = eV$ [SS: Need to remove eV in this derivation]

We can see that there is no choice of $\dot{\varphi}_{\pm}$ such that the parasitic coupling between the readout resonator and fluxonium can be cancelled without eliminating the coupling between the qubit and readout resonator. Note that, $\frac{N+1}{E_g} = \frac{1}{E_g} - \frac{1}{E_c}$ [SS: weird!], and thus, the coupling between the qubit and the readout is same as the parallel circuit if $E_g \ll E_c$ with a lower N. We drive the readout resonator, such that, $\dot{\varphi}_{-} \equiv 2eV$ (the sign of the voltage value has been changed because in this circuit φ_{-1} will be connected to V and not $-V$, just for simplicity).

$$
\mathcal{L} = \frac{\dot{\varphi}_{+}^2}{64 E_c}\Big(2 + \frac{(N+1)E_t}{E_g}\Big) + \frac{\dot{\varphi}_{+} eV}{16 E_c}\Big(\frac{3}{2} + \frac{E_t}{E_c}\Big)
$$
$$
- \frac{(N+1)E_t}{32 E_g E_c}\dot{\phi} eV + \frac{(N+1)E_t}{64 E_g E_c}\dot{\phi}\dot{\varphi}_{+}
$$
$$
- \frac{E_t}{16 E_g E_c}\sum_{\mu}\frac{c_\mu o_\mu}{\sqrt{2N}s_\mu^2}\dot{\xi}_\mu eV
$$
$$
+ \frac{E_t}{32 E_g E_c}\sum_{\mu}\frac{c_\mu o_\mu}{\sqrt{2N}s_\mu^2}\dot{\xi}_\mu\dot{\varphi}_{+} + \mathcal{O}(e^2 V^2)
$$
$$
+ \Big[(M_{00} + G_{00})\dot{\phi}^2 + 2\sum_{\mu}(M_{0\mu} + G_{0\mu})\dot{\phi}\dot{\xi}_\mu
$$
$$
+ \sum_{\mu,\nu}(M_{\mu\nu} + G_{\mu\nu})\dot{\xi}_\mu\dot{\xi}_\nu\Big] - \mathcal{U} \tag{A27}
$$

[SS: Correct the derivation in numerics and text to only use grounded resonator and then extend briefly to the floating case. We are ding so by eliminating all terms with E_c^3, E_c^4 and using $\dot{\varphi}_{-2} = 0, \dot{\varphi}_{-1} = -2eV$. Thus, $\varphi_{+} = \varphi_{-} = -2eV$. So this point everything will be correct and we do not need to change the equations for Ec but only for Eg]

$$
= - \frac{(N+1)E_t}{16 E_g E_c}\dot{\phi} eV - \frac{E_t}{8 E_g E_c}\sum_{\mu}\frac{c_\mu o_\mu}{\sqrt{2N}s_\mu^2}\dot{\xi}_\mu eV
$$
$$
+ \Big[(M_{00} + G_{00})\dot{\phi}^2 + 2\sum_{\mu}(M_{0\mu} + G_{0\mu})\dot{\phi}\dot{\xi}_\mu
$$
$$
+ \sum_{\mu,\nu}(M_{\mu\nu} + G_{\mu\nu})\dot{\xi}_\mu\dot{\xi}_\nu\Big] - \mathcal{U} \tag{A28}
$$

e. Hamiltonian: We will now use Legendre transformation to obtain Hamiltonian variables,

$$
p_\phi = \frac{\partial \mathcal{L}_{\kappa_o}}{\partial \dot{\phi}} = 2(M_{00} + G_{00})\dot{\phi} + \sum_{\mu}(M_{\mu 0} + G_{\mu 0})\dot{\xi}_\mu
$$
$$
- \frac{(N+1)E_t}{16 E_g E_c}eV \tag{A29}
$$

$$
p_{\xi_\mu} = \frac{\partial \mathcal{L}_{\kappa_o}}{\partial \dot{\xi}_\mu} = (M_{0\mu} + G_{0\mu})\dot{\phi} + 2\sum_{\nu}(M_{\mu\nu} + G_{\mu\nu})\dot{\xi}_\nu
$$
$$
- \frac{E_t}{8 E_g E_c}\sum_{\mu}\frac{c_\mu o_\mu}{\sqrt{2N}s_\mu^2}eV \tag{A30}
$$

[SS: define odd and even sectors and then check what is different here.] Here, the even and odd sectors are not decoupled due to the eV term. The even and odd sectors can be diagonalized independently, such

that a rotation on the odd sectors does not affect the even sectors. This is contrary to the case of Eq. 77 in [29] where the rotation of odd sectors affects the even sectors. This is because in that case $G_{0\mu}$ was changed to being dependent on odd as well as even sectors. However, here, only the $\mathcal{L}_V$ term has changed. Thus, if the following condition is satisfied,

$$
\frac{\tilde{E}_c^\phi \tilde{E}_{c,j}^e c_i c_j}{32 N E_g^2 s_i^2 s_j^2} \ll 1 \implies \frac{4 E_g \tilde{E}_c^\phi c_i c_j}{32 N E_g^2 s_i^2} \ll 1 \tag{A31}
$$
$$
\implies \frac{4\tilde{E}_c^\phi N}{8 E_g \pi^2 \mu\nu} \ll 1 \implies N \ll 8\pi^2\frac{E_g}{\tilde{E}_c^\phi}, \tag{A32}
$$

[SS: quote the N] we can carry out the exact same procedure as Ref. [29] to simplify the inversion of matrix for the Legendre transformation and obtain the Hamiltonian as follows. Thus, we arrive at the following Hamiltonian

$$
H_2 = 4\bar{E}_c^\phi p_\phi^2 + \sum_{\mu=1}^{N-1} 4\tilde{E}_{c,\mu}^{e/o} p_\mu^2
$$
$$
+ 2\sum_{\mu=1}^{N-1}\frac{\bar{E}_c^\phi \tilde{E}_{c,\mu}^{e/o} c_\mu o_{\mu+1}}{\sqrt{2N}E_g s_\mu^2}p_\phi p_\mu
$$
$$
- \bar{E}_c^\phi p_\phi eV\Big[\frac{(N+1)E_t}{2 E_g E_c} + \frac{E_t^2 \tilde{E}_{c,\mu}^{e/o}}{8 E_g^2 E_c^2}\Big(\frac{c_\mu^2 o_\mu}{2N s_\mu^4}\Big)\Big]
$$
$$
- \sum_{\mu=1}^{N-1}\frac{\bar{E}_c^\phi \tilde{E}_{c,\mu}^{e/o} c_\mu o_{\mu+1}}{\sqrt{2N}E_g s_\mu^2}\Big[\frac{(N+1)E_t}{8 E_g E_c}\Big]p_\mu eV
$$
$$
+ E_{J_p}\cos\phi + \frac{E_L}{2}\phi^2 + \frac{E_{J_j}}{2}\sum_{\mu=1}^{N-1}\xi_\mu^2 - \frac{\varphi_{-}^2}{16 E_R} \tag{A33}
$$

[SS: Connect this Hamiltonian to the original Hamiltonian and give the expression for each term.] where the variables $\tilde{E}_{c,\mu}^e$ are the same as before and $\tilde{E}_{c,\mu}^o$ is the diagonalized charging energy of odd sectors. Here, $\tilde{E}_{c,\mu}^{e/o}$ denotes that the term will be $\tilde{E}_{c,\mu}^o$ for odd μ and $\tilde{E}_{c,\mu}^e$ for even μ. Thus, we can see that by not preserving the symmetry we only have the extra odd sector term interacting with the readout resonator. However, this term is extremely small [ER: proportional to / why small]. Additionally, $\mathcal{U}$ remains the same as the parallel case. Thus, in terms of types of couplings there might not be major differences, however, the value of $\bar{E}_c^\phi = (G_{00} + M_{00})^{-1}$ changes since G_{00} has changed. This change can also be diminished with increasing N. Thus, for large enough N, this circuit is the same as the parallel circuit.

2. Grounded Fluxonium Circuit

[SS: only express initial Lagrangian upto showing the symmetry is preserved and then show the Hamiltonian] For H_3, the constraint $\dot{\varphi}_N = 0$ yields

$$
\mathcal{L} = \mathcal{L}_{phase-slip} + \mathcal{L}_{JJA} + \mathcal{L}_g + \mathcal{L}_R + \mathcal{L}_C \tag{A34}
$$

$$\mathcal{L}_{phase-slip} = \frac{\dot{\varphi}_0^2}{16E_{C'}} - E_{J_p}\cos(\varphi_0 + \varphi_{\text{ext}}) \qquad (A35)$$

$$\mathcal{L}_{JJA} = \sum_{n=1}^{N} \frac{(\dot{\varphi}_n - \dot{\varphi}_{n-1})^2}{16E_{C_j}^n} - E_{J_j}^n \cos(\varphi_n - \varphi_{n-1}) \qquad (A36)$$

$$\mathcal{L}_R = \frac{\dot{\varphi}_-^2}{16E_R} - \frac{\varphi_-^2}{16E_R} \qquad (A37)$$

$$\mathcal{L}_g = \sum_{n=0}^{N-1} \frac{\dot{\varphi}_n{}^2}{16E_g^n} \qquad (A38)$$

Here, we will not assume that the capacitances to transmission line are infinite or that ground capacitance for the phase-slip junction and JJA. We will leave the value of $\varphi_\pm$ a variable in this case unlike the parallel circuit study we performed above. The grounding of fluxonium yields an additional condition to the fluxoid condition $\varphi_N = c$, a constant which implies that

$$\varphi_0 = c - \sum_{l=1}^{N} \theta_l \implies \dot{\varphi}_0 = -\sum_{l=1}^{N} \dot{\theta}_l \qquad (A39)$$

This used to be our qubit in the definition of collective modes in this article. However, in this case there are only $N-1$ modes, such that the collective modes are defined as,

$$\phi = c + \sum_{l=1}^{N-1} \theta_l \implies \dot{\phi} = -\dot{\varphi}_0 \qquad (A40)$$

Since one of the dynamic variables are fixed we only have $N-1$ modes, thus,

$$\mathcal{L}_{phase-slip} = \frac{(\sum_{m=1}^{N-1}\dot{\theta}_m)^2}{16E_{C'}} + E_{J_p}\cos\Big(\sum_{m=1}^{N}\theta_m + \varphi_{\text{ext}}\Big) \qquad (A41)$$

$$\mathcal{L}_{JJA} = \sum_{n=1}^{N-1} \frac{\dot{\theta}_n^2}{16E_{C_j}^n} - E_{J_j}^n \cos\theta_n \qquad (A42)$$

$$\mathcal{L}_R = \frac{(\dot{\varphi}_{-1} - \dot{\varphi}_{-2})^2}{16E_R} - \frac{(\varphi_{-1} - \varphi_{-2})^2}{2L_R} \qquad (A43)$$

$$\mathcal{L}_g = \frac{\dot{\varphi}_0^2}{16E_g^0} + \sum_{n=1}^{N} \frac{(\dot{\varphi}_0 + \sum_{m=1}^{n}\dot{\theta}_m)^2}{16E_g^m} \qquad (A44)$$

$$= \frac{\dot{\varphi}_0^2}{16E_g^0} + \sum_{n=1}^{N} \frac{1}{16E_g^n}(\dot{\varphi}_0^2 + 2\dot{\varphi}_0\sum_{m=1}^{n}\dot{\theta}_m$$
$$+ \sum_{i=1}^{n}\sum_{j=1}^{n}\dot{\theta}_i\dot{\theta}_j) \qquad (A45)$$

$$= \dot{\varphi}_0^2\sum_{n=0}^{N}\frac{1}{16E_g^n} + 2\sum_{n=1}^{N}\sum_{m=1}^{n}\frac{\dot{\varphi}_0\dot{\theta}_m}{16E_g^n}$$
$$+ \sum_{n=1}^{N}\sum_{j=1}^{n}\sum_{i=1}^{n}\frac{\dot{\theta}_i\dot{\theta}_j}{16E_g^n} \qquad (A46)$$

$$\mathcal{L}_c = \frac{\dot{\varphi}_0^2}{16E_c^1} + \frac{\dot{\varphi}_{-1}^2}{16}\Big(\frac{1}{E_c^1} + \frac{1}{E_c^3}\Big)$$

$$+ \frac{\dot{\varphi}_{-2}^2}{16}\Big(\frac{1}{E_c^4} + \frac{1}{E_c^2}\Big) + \frac{(\dot{\varphi}_0 + \sum_{m=1}^{N}\dot{\theta}_m)^2}{16E_c^2}$$
$$- \frac{\dot{\varphi}_0\dot{\varphi}_{-1}}{8E_c^1} - \frac{\dot{\varphi}_{-2}(\dot{\varphi}_0 + \sum_{m=1}^{N}\dot{\theta}_m)}{8E_c^2}$$
$$- \frac{\dot{\varphi}_{-2}eV}{8E_c^4} + \frac{\dot{\varphi}_{-1}eV}{8E_c^3} \qquad (A47)$$

The term $\frac{(\dot{\varphi}_{-2})^2}{16E_c^4}$ will be added to the Lagrangian. The coupling constant for this case is,

$$\mathcal{L}_c = \frac{(\dot{\varphi}_{-1} - \dot{\varphi}_0)^2}{16E_c^1} + \frac{(\dot{\varphi}_{-1} - eV)^2}{16E_c^3} + \frac{(\dot{\varphi}_{-2})^2}{16E_c^4}, \qquad (A48)$$

$$\mathcal{L} = \frac{\dot{\varphi}_+^2}{16E_c}\Big(2 + \frac{NE_t}{E_g}\Big) - \frac{\dot{\varphi}_+eV}{4E_c}\Big(\frac{3}{8} + \frac{E_t}{E_c}\Big)$$
$$- \frac{NE_t}{16E_gE_c}\dot{\phi}eV - \frac{NE_t}{32E_gE_c}\dot{\phi}\dot{\varphi}_+ \qquad (A49)$$

$$- \frac{E_t}{8E_gE_c}\sum_\mu \frac{c_\mu o_\mu}{\sqrt{2(N-1)}s_\mu^2}\dot{\xi}_\mu eV$$
$$- \frac{E_t}{8E_gE_c}\sum_\mu \frac{c_\mu o_\mu}{\sqrt{2(N-1)}s_\mu^2}\dot{\xi}_\mu\dot{\varphi}_+ + \mathcal{O}(e^2V^2) \qquad (A50)$$

$$+ \Big[(M_{00} + G_{00})\dot{\phi}^2 + 2\sum_\mu(M_{0\mu} + G_{0\mu})\dot{\phi}\dot{\xi}_\mu$$
$$+ \sum_{\mu,\nu}(M_{\mu\nu} + G_{\mu\nu})\dot{\xi}_\mu\dot{\xi}_\nu\Big] - \mathcal{U} \qquad (A51)$$

a. Hamiltonian: All terms in the Hamiltonian (H_2) can be adopted [ER: what do you mean by adopted?] via $N \to N - 1$. If $C_g^N \neq C_g^1$ then this ground fluxonium and floating fluxonium have a larger difference in terms of frequencies of modes. However, we see that by adjusting the values of the differential capacitance C and coupling capacitances C_c, we can optimize the three circuits to have the same qubit and parasitic mode frequencies. See Fig. 11 and Table V for further details.

Appendix B: Undriven Fluxonium Circuit

In this appendix, we summarize the expressions for coupling strengths and charging energies derived above and compare them for all three circuits. We will also analyze effect of variations in circuit parameters on these quantities. This analysis is used in Sec IV to comment on mitigation strategies for the parasitic effects captured in this work. We also discuss the quantities related to the corresponding dispersive qubit Hamiltonians and give expressions for the dispersive coupling $\chi_{\phi\mu}$ used in Sec. III D. Following the main text, we set $\hbar = 1$.

In Table V we note that in addition to the preserved symmetries which restrict qubit couplings to only even parasitic modes, in all three circuits, the values of parasitic quantities $g_{\phi\mu}, g_{\phi r}, \chi_{\phi\mu}$ for $\mu = 2$ are also very similar. Since the parasitic state transitions (p-MIST) and the post readout parasitic-dephasing are determined predominantly by these quantities only,

Fluxonium Parameters ($\mu = 2$)	Parallel Circuit H_1	Floating Fluxonium H_2	Grounded Fluxonium H_3
$g_{\phi\mu}$	157 GHz	161 GHz	158 GHz
$g_{\mu r}$	4.223 MHz	3.971 MHz	3.128 MHz
$\chi_{\phi,\mu}$	-1.1 MHz	-1.3 MHz	-1.1 MHz

TABLE V. **Parasitic quantities for the mode $\mu = 2$ across various ground configurations shown in Fig. 11(a-c).** The table gives values of coupling strengths between the qubit and the readout $g_{\phi\mu}$, readout and the parasitic-mode $g_{\phi r}$, parasitic-qubit $g_{\mu r}$ and the dispersive shift due to the parasitic mode $\chi_{\phi\mu}$.

this observation leads to our conclusion that the various grounding configurations covered in App. A will have the same Floquet landscape. These arguments hold for all parasitic modes μ as shown by Figs. 11(d) and 15.

1. Charging energies and Coupling Strengths

Here, we summarize the expressions for couplings and charging energies for the three circuits as derived in App. A for circuits in Figs. 11(b,c) and Ref. [29] for circuit in Figs. 11(a). We will use these expressions to show the variations with number of junctions N and parasitic ground capacitance C_g, used in Sec. IV. [SS: check these expressions after derivation. Also multiply the charge fluctuations.]

1. Total ground capacitance.

   (a) $H_1 : E_t = \left(\frac{N-1}{E_g} + \frac{2}{E_{g1}} + \frac{2}{E_c}\right)^{-1} = 0.57$ GHz

   (b) $H_2 : E_t = \left(\frac{N-1}{E_{g,j}} + \frac{2}{E_{gp}} + \frac{1}{E_c}\right)^{-1}$

   (c) $H_3 : E_t = \left(\frac{N-1}{E_{g,j}} + \frac{1}{E_{gp}} + \frac{1}{E_c}\right)^{-1}$

2. Qubit Charging energy $(4E_c^\phi \hat{N}_\phi^2)$.

   (a) $H_1 : \bar{E}_c^\phi = \left(\frac{1}{4E_t}\left(1 - \frac{2}{3}\frac{(N+1)(N-1)}{N}\frac{E_t}{E_g}\right) + \frac{1}{E_{C'}} + \frac{1}{NE_{C_j}}\right)^{-1} = 0.92$ GHz.

   (b) $H_2 : \bar{E}_c^\phi = \left(\frac{1}{4E_t}\left(1 - \frac{E_t}{E_c}\right)^2\left[1 - \frac{2}{3}\frac{N-1}{N}\right] + \frac{1}{E_{C_p}} + \frac{1}{NE_{C_j}}\right)^{-1}$.

   (c) $H_3 : \bar{E}_c^\phi = \left(\frac{1}{4E_t}\left(1 - \frac{E_t}{E_c}\right)^2\left[1 - \frac{2}{3}\frac{N-2}{N-1}\right] + \frac{1}{E_{C_p}} + \frac{1}{NE_{C_j}}\right)^{-1}$.

3. Even Parasitic Mode Charging Energy $(4E_{c,\mu}^e \hat{N}_\mu^2)$.

   (a) $H_1 : \tilde{E}_{c,\mu}^e = \left(\frac{1}{E_{C_j}} + \frac{1}{4E_g s_\mu^2}\right)^{-1}$

   (b) H_2 : Same as H_1

   (c) H_3 : Same as H_1

4. Qubit-Readout Coupling $(g_{\phi r}N_{\phi,\mathrm{ZPF}}N_{\mu,\mathrm{ZPF}})$.

   (a) $H_1 : \frac{\tilde{E}_c^\phi}{E_c}$

(b) $H_2 : \frac{\bar{E}_c^\phi}{E_c}\left[\frac{(N+1)E_t}{2E_{g,j}} + \frac{E_t^2 \tilde{E}_{c,\mu}^o}{8E_{g,j}^2 E_c}\left(\frac{c_\mu^2}{2Ns_\mu^4}\right)\right]$

(c) $H_3 : \frac{\bar{E}_c^\phi}{E_c}\left[\frac{NE_t}{2E_{g,j}} + \frac{E_t^2 \tilde{E}_{c,\mu}^o}{8E_{g,j}^2 E_c}\left(\frac{c_\mu^2}{2(N-1)s_\mu^4}\right)\right]$

5. Qubit-Parasitic Coupling $(g_{\phi\mu}N_{\phi,\mathrm{ZPF}}N_{\mu,\mathrm{ZPF}})$

   (a) $H_1 : \sqrt{\frac{2}{N}}\frac{\tilde{E}_c^\phi \tilde{E}_{c,\mu}^e c_\mu}{E_{g,j}s_\mu^2}$

   (b) $H_2 : \sqrt{\frac{2}{N}}\frac{\bar{E}_c^\phi \tilde{E}_{c,\mu}^e c_\mu}{E_{g,j}s_\mu^2}$

   (c) $H_3 : \sqrt{\frac{2}{N-1}}\frac{\bar{E}_c^\phi \tilde{E}_{c,\mu}^e c_\mu}{E_{g,j}s_\mu^2}$

6. Readout-Parasitic Coupling $(g_{\mu r}N_{\mu,\mathrm{ZPF}}V_{\mathrm{ZPF}})$

   (a) $H_1 : \frac{\tilde{E}_c^\phi \tilde{E}_{c,\mu}^e c_\mu}{4\sqrt{2N}E_{g,j}E_c s_\mu^2}$

   (b) $H_2 : \frac{\bar{E}_c^\phi \tilde{E}_{c,\mu}^e c_\mu}{4\sqrt{2N}E_{g,j}s_\mu^2 E_c}\left[\frac{(N+1)E_t}{2E_g}\right]$

   (c) $H_3 : \frac{\bar{E}_c^\phi \tilde{E}_{c,\mu}^e c_\mu}{4\sqrt{2(N-1)}E_{g,j}s_\mu^2 E_c}\left[\frac{NE_t}{2E_{g,j}}\right]$

Zooming into Fig. 11(c), we can see in Fig. 12 that for all three circuits the lowest three even modes $\mu = 2, 4, 6$ couple to the qubit stronger than the readout. This observation is a backbone of our work; we find that because of this relatively large coupling strength, p-MIST rates may be significant in a broader fluxonium-based quantum computers.
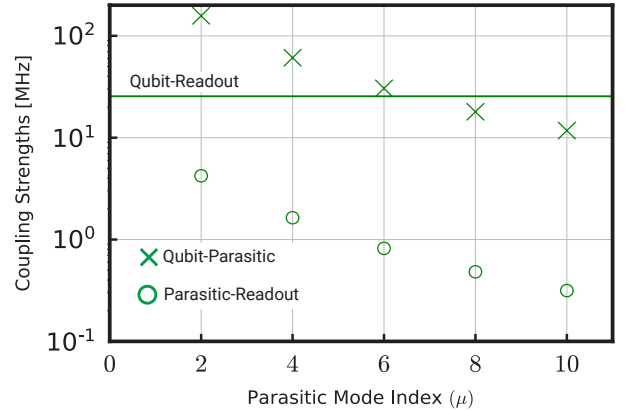

FIG. 12. **Absolute values of the coupling strengths.** $g_{\phi r}/2\pi$ (qubit-readout), $g_{\phi\mu}/2\pi$ (qubit-parasitic), $g_{\mu r}/2\pi$ (parasitic-readout), for various circuits. Coupling to odd parasitic modes is zero due to the symmetries of the circuit [29]. The parasitic modes $\mu \in \{2, 4, 6\}$ couple to the qubit more strongly than the readout.

a. Variations with circuit parameters: In Fig. 13, we show the dependence of charging energies and coupling constants on the number of junctions N as well as the ground capacitance C_g. We find that the charging energies increase with decrease in C_g and N. The parasitic charging energy is crucial in deciding the parasitic mode frequency ω_μ. A higher parasitic charging frequency relative to the readout frequency can lower the chances of p-MIST effects. Thus, we prefer large C_g and N. The coupling strengths as shown in Fig. 7 induce all MIST effects. In particular, the parasitic-qubit coupling $g_{\phi\mu}$ is responsible for p-MIST effects. The parasitic-readout coupling $g_{\mu r}$ on the other hand

only increases population of the parasitic modes and is directly proportional to $g_{\phi\mu}$. We find that for low $g_{\phi\mu}$ a low C_g and high N is required. Thus, to reduce p-MIST effects the best strategy is to target for low parasitic ground capacitance in the JJA and high junction count.
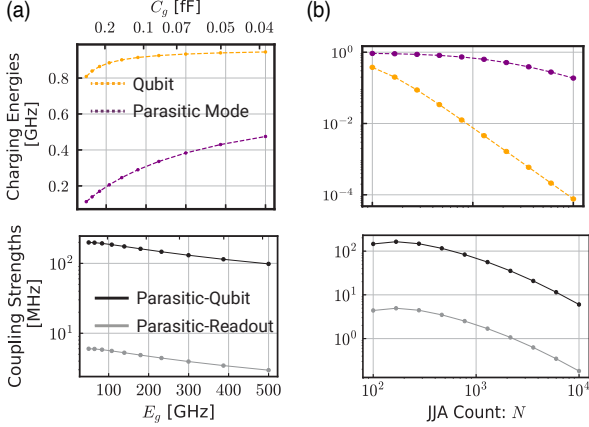

FIG. 13. **Dependence of coupling strengths and charging energies on circuit parameters.** (a) parasitic ground capacitance and (b) number of junctions in the array N. **(Top row)** The qubit charging energy decides the frequency ω_{01} and the parasitic charging energy decides the parasitic mode frequency for mode $\mu = 2$. **(Bottom row)** give the plots for the coupling strengths of the parasitic mode to readout and qubit, respectively. All plots are obtained under linear JJA approximation.

2. Fluxonium Qubit Hamiltonian

We now discuss the Fluxonium qubit Hamiltonian, through a detailed consideration of its charge matrix elements and the dispersive shifts on the qubit induced by the parasitic modes and readout. This dispersive Hamiltonian is derived using the Schrieffer-Wolff approximation [29]. The qubit Hamiltonian H_ϕ (see Eq. 2) is diagonalized in the Fock state basis, where we have used the standard bosonic operators

$$\hat{x} = x_{\text{ZPF}}(a + a^\dagger) = \hat{N}_\phi / N_{\phi,\text{ZPF}} \qquad \text{(B1)}$$

and

$$\hat{p} = -ip_{\text{ZPF}}(a - a^\dagger) = \hat{\phi}/\phi_{\text{ZPF}}. \qquad \text{(B2)}$$

a. *Charge Matrix Elements for H_1, H_2, H_3:* Here, using the approximations described in App. A, we calculate the charge matrix elements for the qubit mode. We observe that with increasing final state (f), the charge matrix elements with respect to the ground and first excited states follow a decreasing trend, approximately exponential. This exponential decrease to 10^{-10} motivates our truncation of the fluxonium potential up to 30 levels for the Floquet simulations of Sec. III.

b. *Dispersive Hamiltonian* We use the Schrieffer-Wolff approximation to extract the readout parameters in Table II, for example, the dispersive shift of the qubit due to the parasitic modes $\chi_{\phi\mu}$ and the readout
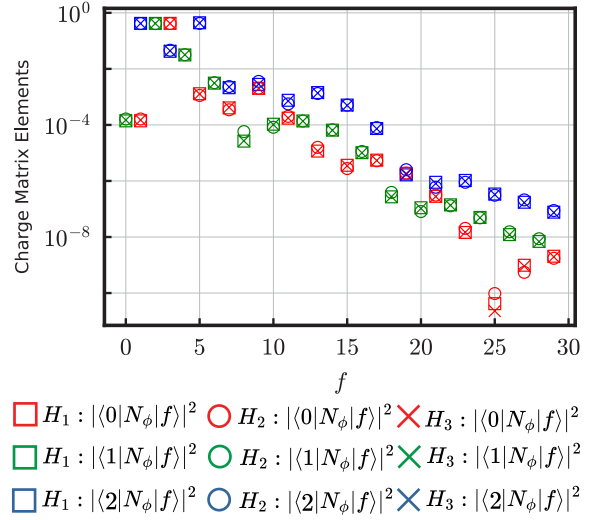

FIG. 14. **Charge Matrix Elements (squared) for all three circuits.** Note that in the equations below we substitute $\langle f|N_\phi|f'\rangle = iN_{\phi,\text{ZPF}}\langle f|(a - a^\dagger)|f'\rangle$ where $N_{\phi,\text{ZPF}} = \frac{1}{\sqrt{2}}\left(E_{J,j}/8NE_C\right)^{1/4}$. The charge matrix elements between odd-odd or even-even is zero (points not seen in log plot) due to the symmetry of cosine potential at $\varphi_{\text{ext}} = 0.5\Phi_0$, where Φ_0 is the flux quantum.

mode $\chi_{\phi r}$ [29]. (These variables were used to generate Fig. 6 in the main text). The Hamiltonian is

$$H/\hbar = \frac{\omega_q}{2}\sigma_z + \sum_\mu(\omega_\mu + k_\mu)a_\mu^\dagger a_\mu + \omega_r a_r^\dagger a_r$$
$$+ \chi_{r,\phi}\sigma_z a_r^\dagger a_r + \sum_\mu \chi_{\mu,\phi}\sigma_z a_\mu^\dagger a_\mu$$
$$+ \sum_\mu \chi_{r\mu} a_\mu^\dagger a_\mu a_r^\dagger a_r \qquad \text{(B3)}$$
$$= \frac{\omega_q}{2}\sigma_z + \left(\omega_r + \chi_{r\phi}\sigma_z\right)a_r^\dagger a_r$$
$$+ \sum_\mu\left(\omega_\mu + k_\mu + \chi_{r\mu}a_r^\dagger a_r + \chi_{\mu\phi}\sigma_z\right)a_\mu^\dagger a_\mu$$
$$\text{(B4)}$$

where $\quad \omega_q$ or $\omega_{01} = \epsilon_0 - \epsilon_1$

$$+ |\langle 0|p_\phi|1\rangle|^2\left[16g_{r\phi}^2 E_{C_r}^2\sqrt{\frac{E_{L_r}}{32E_{C_r}}}\frac{2\epsilon_{01}}{\epsilon_{01}^2 - \omega_r^2}\right.$$
$$+ \sum_\mu\left\{g_{\mu\phi}^2\sqrt{\frac{E_{J_j}}{32\tilde{E}_{C,\mu}^e}}\frac{2\epsilon_{01}}{\epsilon_{01}^2 - \omega_\mu^2}\right\}\right]$$
$$+ \sum_{l>1}16g_{r\phi}^2 E_{C_r}^2\sqrt{\frac{E_{L_r}}{32E_{C_r}}}\left[\frac{|\langle 0|p_\phi|l\rangle|^2}{\epsilon_{0l} - \omega_r}\right.$$
$$- \frac{|\langle 1|p_\phi|l\rangle|^2}{\epsilon_{1l} - \omega_r}\right] + \sum_{l>1,\mu}\left\{g_{\mu\phi}^2\sqrt{\frac{E_{J_j}}{32\tilde{E}_{C,\mu}^e}}\times\right.$$
$$\left.\left[\frac{|\langle 0|p_\phi|l\rangle|^2}{\epsilon_{0l} - \omega_\mu} - \frac{|\langle 1|p_\phi|l\rangle|^2}{\epsilon_{1l} - \omega_\mu}\right]\right\} \qquad \text{(B5)}$$
$$k_{\mu\in 2\mathbb{Z}} = 16E_{C_r}^2\sqrt{\frac{E_{L_r}}{32E_{C_r}}}\sqrt{\frac{E_{J_j}}{32E_C^e}}\left[\frac{g_{r\mu}^2}{\omega_\mu - \omega_r}\right]$$

$$\leq \mathcal{O}(10^{-8}) \tag{B6}$$

$$\chi_{r,\phi} = 16 g_{r\phi}^2 E_{C_r}^2 \sqrt{\frac{E_{L_r}}{32 E_{C_r}}} \frac{2\epsilon_{01}}{\epsilon_{01}^2 - \omega_r^2} |\langle 0|p_\phi|1\rangle|^2$$

$$+ 16 g_{r\phi}^2 E_{C_r}^2 \sqrt{\frac{E_{L_r}}{32 E_{C_r}}} \left[\sum_l |\langle 0|p_\phi|l\rangle|^2 \frac{\epsilon_{0l}}{\epsilon_{0l}^2 - \omega_r^2} \right.$$

$$\left. - \sum_l |\langle 1|p_\phi|l\rangle|^2 \frac{\epsilon_{1l}}{\epsilon_{1l}^2 - \omega_r^2} \right] \tag{B7}$$

$$\chi_{\mu,\phi} = g_{\mu\phi}^2 \sqrt{\frac{E_{J_j}}{32 \tilde{E}_{C,\mu}^e}} \frac{2\epsilon_{01}}{\epsilon_{01}^2 - \omega_\mu^2} |\langle 0|p_\phi|1\rangle|^2$$

$$+ g_{\mu\phi}^2 \sqrt{\frac{E_{J_j}}{32 \tilde{E}_{C,\mu}^e}} \left[\sum_l |\langle 0|p_\phi|l\rangle|^2 \frac{\epsilon_{0l}}{\epsilon_{0l}^2 - \omega_\mu^2} \right.$$

$$\left. - \sum_l |\langle 1|p_\phi|l\rangle|^2 \frac{\epsilon_{1l}}{\epsilon_{1l}^2 - \omega_\mu^2} \right] \quad \text{(see Fig. 15)} \tag{B8}$$

For the parameters in Table I, $\omega_q = \omega_{01} = -30$ MHz while $\chi_{\mu,\phi}$ is shown in Fig. 15.
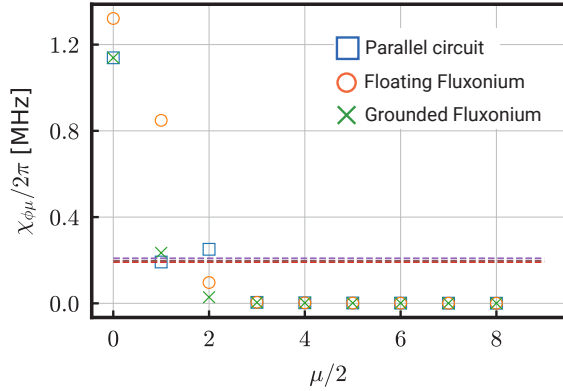

FIG. 15. **The dispersive shift induced on the qubit due to the parasitic mode μ.** The three grounding configurations, parallel circuit (H_1), floating Fluxonium (H_2), and grounded fluxonium (H_3) shown in Figs. 13(a-c) yield the same values. Dashed lines in the same color code represent the dispersive shift ($\sim$) induced by the readout resonator on the qubit.

Appendix C: Driven Fluxonium Circuit

Here, we discuss several analysis techniques. We begin with the derivation of $H_{s.c.}$ in Eq. 6. Then we discuss and justify the Hilbert space truncation, as well as approximations used for Floquet simulations in Sec. III.

1. Semi-classical Approximation

2. Approximations for Numerical Modeling

We use the following three approximations in our work.

- **Restriction to** $\mu = 2$. We restrict our analyses to only include the lowest-frequency, even parasitic mode. This mode couples most strongly to the qubit and the readout as evident from Fig. 12(d). This assumption reduces the Hilbert space size for feasible study.

- **Semi-classical drive approximation.** We treat the readout resonator classically as described in Refs. [20–23], eliminating the readout mode states from our numerical simulation. This approximation is again necessary to restrict the Hilbert space size to values feasible for numeric study.

- **Linear JJA Approximation.** We assume that the parasitic modes are linear, due to the large $E_{J_j}/E_{C_j} \sim 200$ ratio. Nonlinear corrections to our results is beyond the scope of this work. For details on how nonlinear corrections affect different circuit energies, we direct the readers to Ref. [29].

Finally, we note that the charge matrix elements connecting the fluxonium qubit ground states to excited states decreases roughly exponentially with increasing excited state number. With this observation, shown in Fig. 14, as well as our assumptions above, we truncate the Hilbert space dimensions to $30 \otimes 10$. That is, we assume 30 levels in the fluxonium qubit mode and 10 levels in the parasitic mode. In the presence of parasitic mode nonlinearity, the Hilbert size would need to be much larger to capture the required effects. Note that for the conclusions drawn in this paper, we are only interested in identifying the existence of p-MIST processes, and do not claim to quantify how many such transitions can be present. Hence, with this truncation we only examine the excitations to $0 - 2$ levels in the parasitic mode and $0 - 20$ in the fluxonium subspace in Figs. 3, 9, 7. For more details, see App. B.

[SS: Include the 30 X 10 as well as 20 X 3]

3. Floquet Simulations

a. Stark shift: To observe a state transition the primary requirements are high charge matrix elements and low energy difference. The eigen-energies of the states in question are changed with an increase in the number of readout photons or, in this case, the drive strength. In this section, we compute the Stark shifted eigen-energies which facilitates the prediction of an avoided crossing, given $\bar{n}_r, \omega_r$ and the charge matrix elements. Let $|i\rangle$ be a state in the eigenspace of $H_{int} = H_\phi + H_{\mu=2} + g_{\phi\mu}\hat{N}_\phi\hat{N}_\mu$. Following derivations in App. B, the AC Stark-shift in the energy of state $|i\rangle$ at an average number of readout photons $\bar{n}_r$ is given by

$$\chi_i(\bar{n}_r) = 2\bar{n}_r \sum_f \omega_{if} \left[\frac{g_{\phi r}|\langle i|\hat{N}_\phi|f\rangle|^2}{\omega_d^2 - \omega_{if}^2} + \frac{g_{\mu r}|\langle i|\hat{N}_\mu|f\rangle|^2}{\omega_d^2 - \omega_{if}^2} \right] \tag{C1}$$

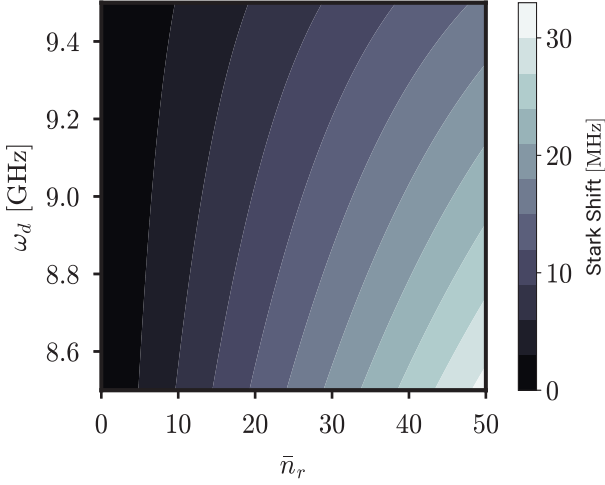FIG. 16. Stark shift in different energy levels for readout computed using Eq. C1 for energy level $|\tilde{0}, \tilde{0}\rangle$. We have verified that stark shift on the excited energy levels $|\tilde{1}, \tilde{0}\rangle$ and $|\tilde{2}, \tilde{0}\rangle$ are also upper bounded by 50 MHz for the ranges considered in x- and y-axes in this plot.

Here $\omega_{if} = E_f - E_i$ denote the energy difference in the eigen-energies of the state $|i\rangle$. The impact due to the second term is much smaller than the first term, and hence $g_{\phi r}$ primarily governs this Stark shift.

b. *Population exchange and quasienergies:* Below we plot the population exchange and quasienergy probabilities for all transitions captured in Fig. 3 and Table III for states $|\tilde{0}, \tilde{0}\rangle$ (see Fig. 20), $|\tilde{1}, \tilde{0}\rangle$ (see Fig. 21) and $|\tilde{2}, \tilde{0}\rangle$ (see Fig. 22).

c. *Landau-Zener probabilities:* We compute the Landau-Zener probabilties in Sec. III C numerically using the quasienergies from the Floquet simulations, and analytically, using the Stark-shifted eigenenergies. In this case, we use a time-dependent readout photon number, where $\bar{n}_r$ varies as $\bar{n}_r = 50(1 - e^{-\kappa t/2})^2$, to emulate change in readout photons from dissipation. The numerical calculations use the probability for Landau-Zener transitions given in [31], for an avoided crossing observed between states $|i\rangle$, $|f\rangle$ of

$$P_{LZ} = \exp\left[-\frac{\pi \Delta_{ac}^2}{2v}\right], \quad \text{(C2)}$$

$$\text{where } v = \sqrt{2\Delta_{ac} \left|\frac{d^2 \epsilon_f}{d\sqrt{\bar{n}_r(t)}^2}\right|_{t_{ac}} \frac{d\sqrt{\bar{n}_r(t)}}{dt}\Big|_{t_{ac}}} \quad \text{(C3)}$$

Here, the variable ϵ_j is the numerically-computed quasi-energy obtained from Floquet simulations, while Δ_{ac} refers to the quasi-energy difference at avoided crossing.

Appendix D: Alternative Circuit

Here, we give the circuit parameters (Table VI), coupling strengths (Fig. 17), charge matrix elements (Fig. 18) and state transition quasienergies shown in Figs. 10 and Fig. 19.

The coupling strengths in this circuit are similar to those evaluated for our original circuit parameters, in Fig. 12.

N	φ_{ext}	E_{J_p}	E_{C_p}	E_C	E_{C_j}	E_{J_j}	$E_{C_{g,j}}$	$E_{C_{g,p}}$	E_c
102	$0.5\Phi_0$	6.20	1.24	4.28	0.74	81.6	194	1.94	19.40

TABLE VI. Circuit parameters for Fig. 10(a) inspired by Ref. [6]. All energies are given in GHz. Here $\Phi_0 = h/2e$ denotes the magnetic flux quantum. The capacitive energies $E_{C'} = \frac{19.4}{C'(fF)}$ GHz are computed from the corresponding capacitances C'.
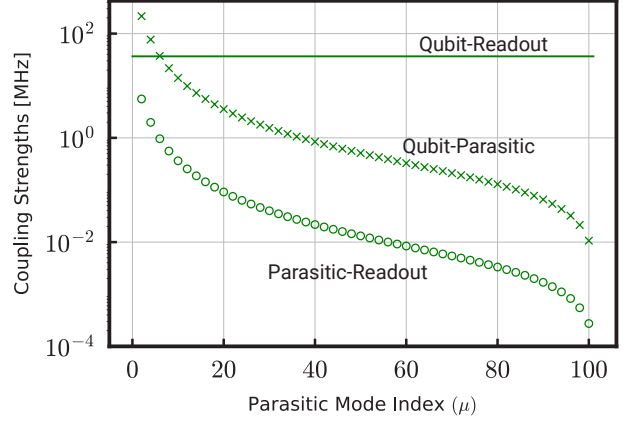

FIG. 17. **Absolute values of the coupling strengths.** $g_{\phi r}/2\pi$ (qubit-readout), $g_{\phi \mu}/2\pi$ (qubit-parasitic), $g_{\mu r}/2\pi$ (parasitic-readout), for various circuits. Coupling to odd parasitic modes is zero due to the symmetries of the circuit [29]. The parasitic modes $\mu \in \{2, 4, 6\}$ couple to the qubit more strongly than the readout.

We find in Fig. 18 that the charge matrix elements of the second circuit analyzed in Sec. IV C has a faster decrease with increasing excited state levels. This could be indicative of the fact that such a circuit will see lower MIST effects as observed in Fig. 10(c).
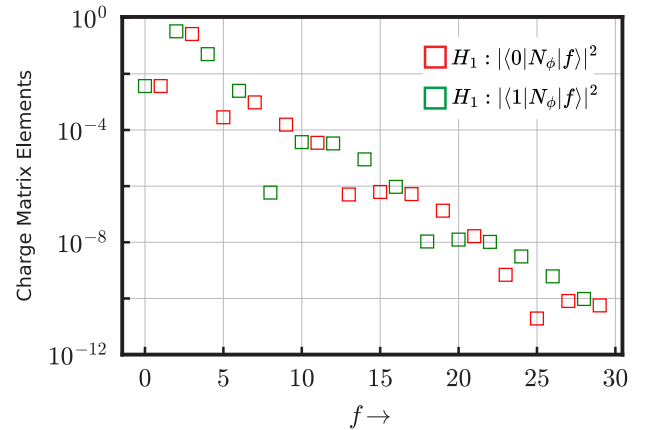

FIG. 18. **Charge Matrix Elements (squared) for all three circuits.** Note that in the equations below we substitute $\langle i|N_\phi|f\rangle = iN_{\phi,\text{ZPF}}\langle i|(a - a^\dagger)|f\rangle$ where $N_{\phi,\text{ZPF}} = \frac{1}{\sqrt{2}}\left(E_{J,j}/8NE_C\right)^{1/4}$. The charge matrix elements between odd-odd or even-even is zero (points not seen in log plot) due to the symmetry of cosine potential at $\varphi_{ext} = 0.5\Phi_0$, where Φ_0 is the flux quantum. Here H_1 denotes the parallel circuit in Fig. 11(a).

Finally, we plot the p-MIST effect observed in

the Floquet simulations for this alternative circuit in Fig. 19. We perform a branch analysis of the initial state $|\tilde{0}, \tilde{0}\rangle$ and observe a transition to $|\tilde{4}\tilde{1}\rangle$, as described in the main text.
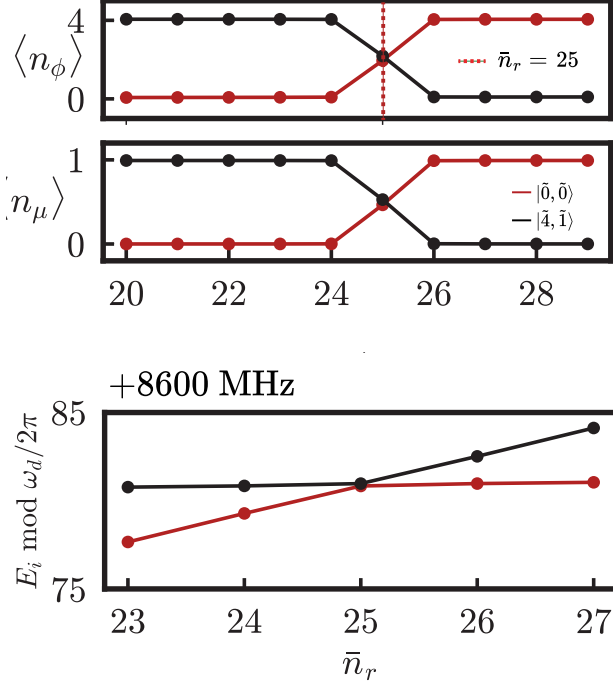

FIG. 19. **Examples of p-MIST using transitions for the alternative circuit in Fig. 10(c) of Sec. IV C.** involving the states $|\tilde{0}, \tilde{0}\rangle \leftrightarrow |\tilde{4}, \tilde{1}\rangle$, with maximum overlap to the un-hybridized state $|k\rangle_\phi \otimes |n\rangle_{\mu=2}$. **Top row:** Qubit mode average occupation $\langle n_\phi \rangle$. **Middle row:** Parasitic mode average occupation $\langle n_\mu \rangle$. **Bottom row:** Quasi-energies (solid) from Floquet simulations showing avoided crossings. Plots are extracted from numerical data used in Fig. 3. The data points are connected by lines for visual aid.
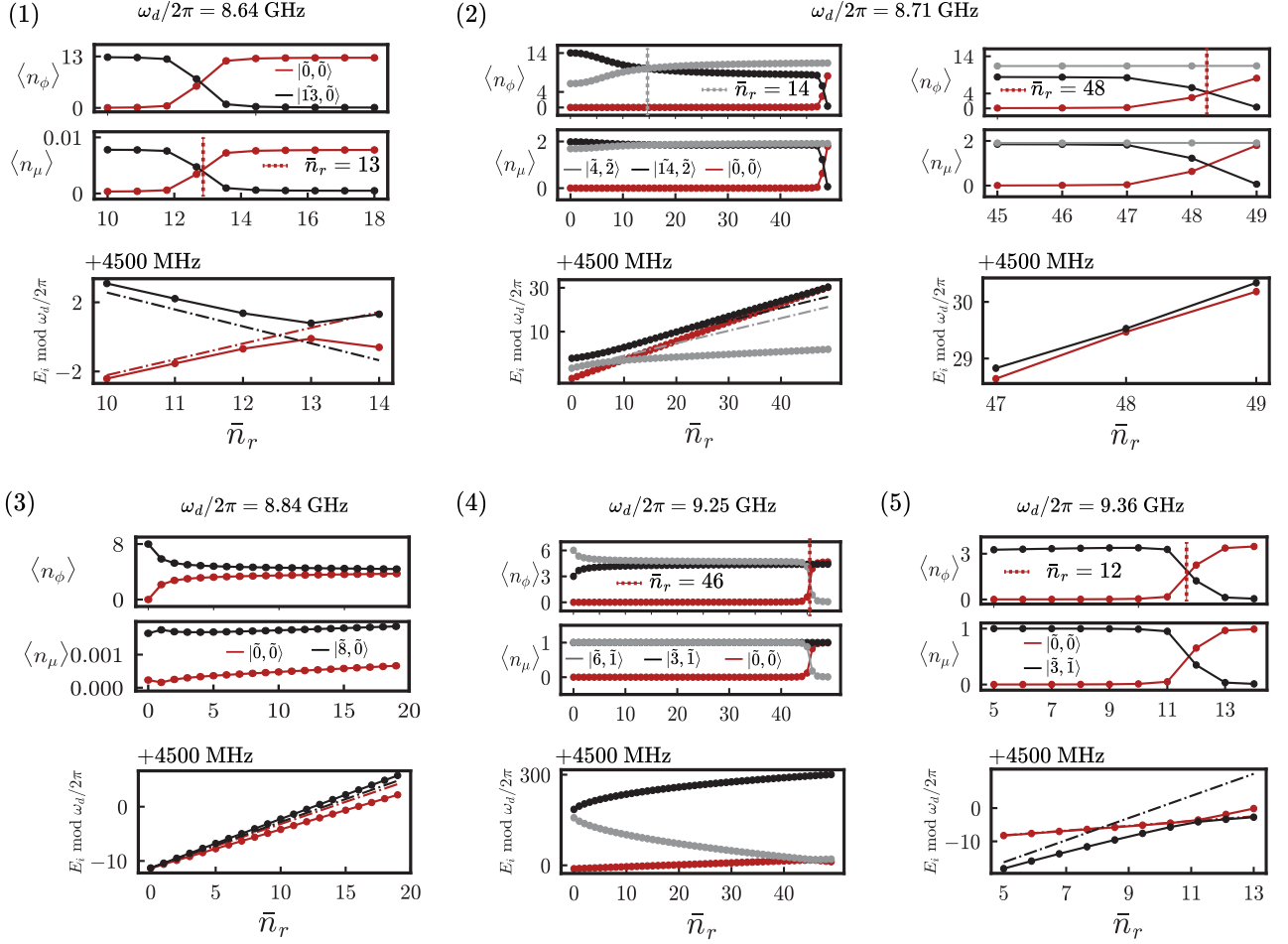
FIG. 20. MIST processes from Table III involving the $|\tilde{0},\tilde{0}\rangle$ state in rows indexed by figure numbering. (Top row) Fluxonium subspace $\langle n_\phi \rangle$. (Middle) Parasitic mode subspace $\langle n_\mu \rangle$ (Bottom) Stark-shifted eigen-energies (dashed) and quasi-energies (solid) from Floquet simulations, corresponding to the initial state i as per the legend. Inset shows avoided crossing of quasi-energies. Floquet results are extracted from numerical data used for Fig. 3. Note that MIST in figure (2) is split into two figures in order to capture the two consecutive transitions involved.
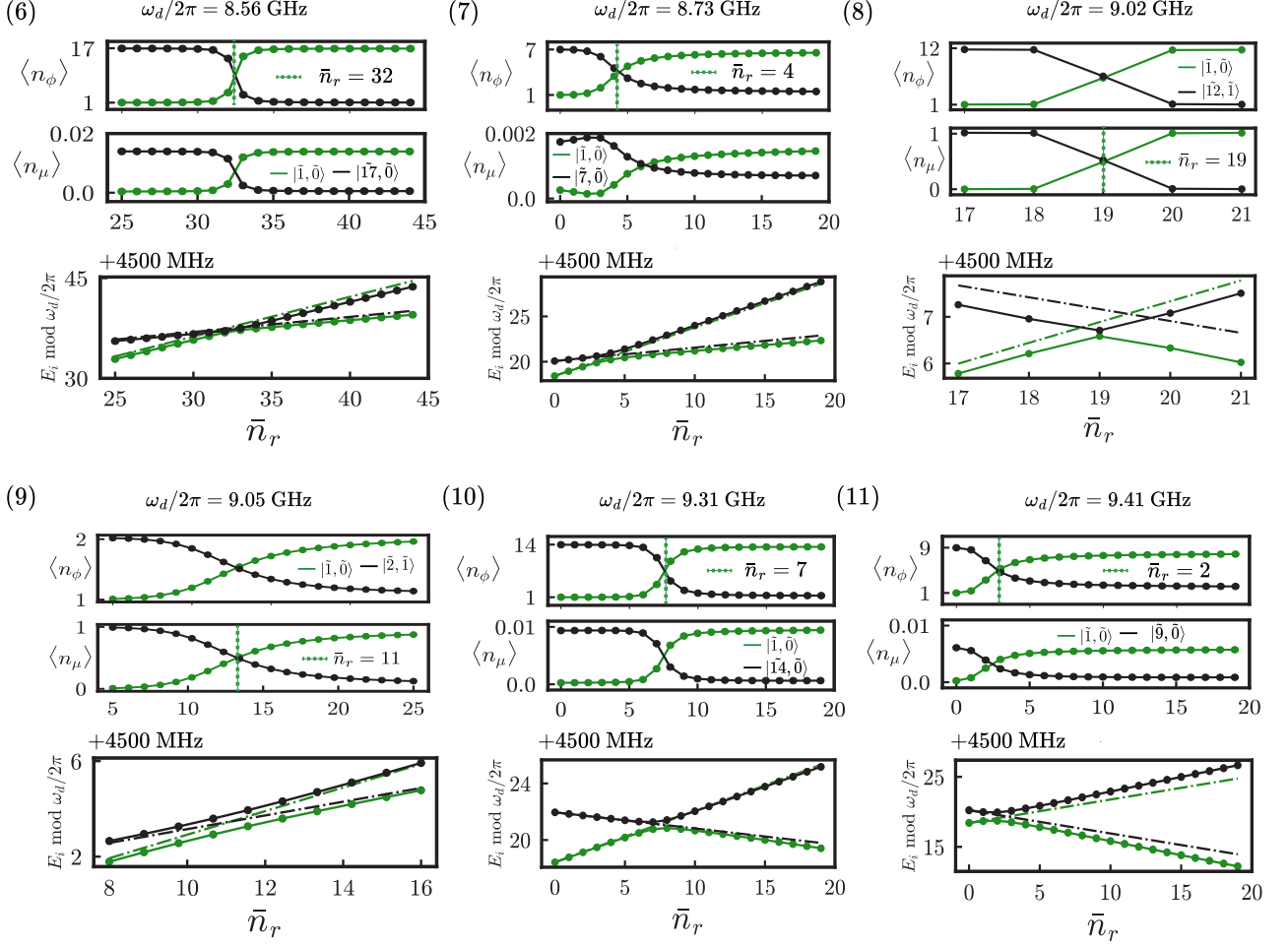
FIG. 21. MIST processes from Table III involving the $|\tilde{1}, \tilde{0}\rangle$ state in rows indexed by figure numbering. (Top row) Fluxonium subspace $\langle n_\phi \rangle$. (Middle) Parasitic mode subspace $\langle n_\mu \rangle$ (Bottom) Stark-shifted eigen-energies (dashed) and quasi-energies (solid) from Floquet simulations, corresponding to the initial state i as per the legend. Inset shows avoided crossing of quasi-energies. Floquet results are extracted from numerical data used for Fig. 3.
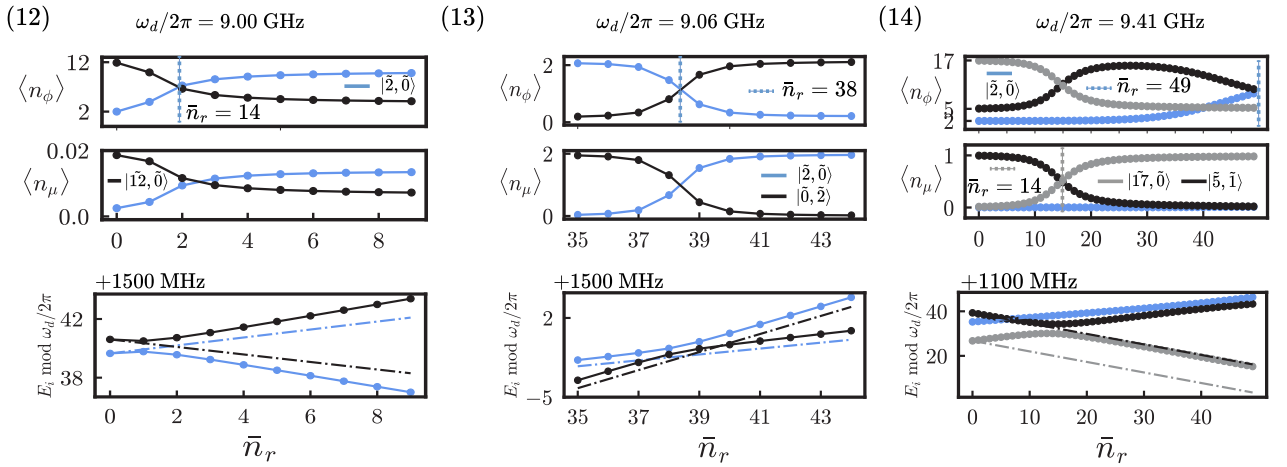

FIG. 22. MIST processes from Table III involving the $|\tilde{2}, \tilde{0}\rangle$ state in rows indexed by figure numbering. (Top row) Fluxonium subspace $\langle n_\phi \rangle$. (Middle) Parasitic mode subspace $\langle n_\mu \rangle$ (Bottom) Stark-shifted eigen-energies (dashed) and quasi-energies (solid) from Floquet simulations, corresponding to the initial state i as per the legend. Inset shows avoided crossing of quasi-energies. Floquet results are extracted from numerical data used for Fig. 3.

- Units of g is an outstanding issue: momentum or charge coefficient?

- p-MIST or PIST

- some sub-figures have subheadings some do not

- shorter conclusion

[1] Phys. Rev. X 9, 041041 (2019) - High-Coherence Fluxonium Qubit (2019).

[2] A. Somoroff, Q. Ficheux, R. A. Mencia, H. Xiong, R. Kuzmin, and V. E. Manucharyan, Millisecond Coherence in a Superconducting Qubit, Physical Review Letters 130, 267001 (2023), publisher: American Physical Society.

[3] Fluxonium: Single Cooper-Pair Circuit Free of Charge Offsets | Science (2009).

[4] N. Earnest, S. Chakram, Y. Lu, N. Irons, R. K. Naik, N. Leung, L. Ocola, D. A. Czaplewski, B. Baker, J. Lawrence, J. Koch, and D. I. Schuster, Realization of a Λ system with metastable states of a capacitively shunted fluxonium, Phys. Rev. Lett. 120, 150504 (2018).

[5] H. Zhang, S. Chakram, T. Roy, N. Earnest, Y. Lu, Z. Huang, D. Weiss, J. Koch, and D. I. Schuster, Universal fast flux control of a coherent, low-frequency qubit, Physical Review X 11, 011010 (2021), arXiv:2002.10653 [cond-mat, physics:quant-ph].

[6] L. Ding, M. Hays, Y. Sung, B. Kannan, J. An, A. Di Paolo, A. H. Karamlou, T. M. Hazard, K. Azar, D. K. Kim, B. M. Niedzielski, A. Melville, M. E. Schwartz, J. L. Yoder, T. P. Orlando, S. Gustavsson, J. A. Grover, K. Serniak, and W. D. Oliver, High-Fidelity, Frequency-Flexible Two-Qubit Fluxonium Gates with a Transmon Coupler, Physical Review X 13, 031035 (2023), publisher: American Physical Society.

[7] H. Zhang, C. Ding, D. Weiss, Z. Huang, Y. Ma, C. Guinn, S. Sussman, S. P. Chitta, D. Chen, A. A. Houck, J. Koch, and D. I. Schuster, Tunable Inductive Coupler for High-Fidelity Gates Between Fluxonium Qubits, PRX Quantum 5, 020326 (2024), publisher: American Physical Society.

[8] K. N. Nesterov, C. Wang, V. E. Manucharyan, and M. G. Vavilov, cnot Gates for Fluxonium Qubits via Selective Darkening of Transitions, Physical Review Applied 18, 034063 (2022), publisher: American Physical Society.

[9] K. N. Nesterov, Q. Ficheux, V. E. Manucharyan, and M. G. Vavilov, Proposal for Entangling Gates on Fluxonium Qubits via a Two-Photon Transition, PRX Quantum 2, 020345 (2021), publisher: American Physical Society.

[10] E. Dogan, D. Rosenstock, L. Le Guevel, H. Xiong, R. A. Mencia, A. Somoroff, K. N. Nesterov, M. G. Vavilov, V. E. Manucharyan, and C. Wang, Two-Fluxonium Cross-Resonance Gate, Physical Review Applied 20, 024011 (2023), publisher: American Physical Society.

[11] E. L. Rosenfeld, C. T. Hann, D. I. Schuster, M. H. Matheny, and A. A. Clerk, Designing high-fidelity two-qubit gates between fluxonium qubits, arXiv preprint arXiv:2403.07242 (2024).

[12] PRX Quantum 3, 037001 (2022) - Blueprint for a High-Performance Fluxonium Quantum Processor (2022).

[13] N. A. Masluk, I. M. Pop, A. Kamal, Z. K. Minev, and M. H. Devoret, Microwave Characterization of Josephson Junction Arrays: Implementing a Low Loss Superinductance, Physical Review Letters 109, 137002 (2012), publisher: American Physical Society.

[14] F. Wang, K. Lu, H. Zhan, L. Ma, F. Wu, H. Sun, H. Deng, Y. Bai, F. Bao, X. Chang, et al., Achieving millisecond coherence fluxonium through overlap josephson junctions, arXiv preprint arXiv:2405.05481 (2024).

[15] A. Blais, A. L. Grimsmo, S. M. Girvin, and A. Wallraff, Circuit quantum electrodynamics, Reviews of Modern Physics 93, 025005 (2021).

[16] D. Gusenkova, M. Spiecker, R. Gebauer, M. Willsch, D. Willsch, F. Valenti, N. Karcher, L. Grünhaupt, I. Takmakov, P. Winkel, et al., Quantum nondemolition dispersive readout of a superconducting artificial atom using large photon numbers, Physical Review Applied 15, 064030 (2021).

[17] U. Vool, A. Kou, W. C. Smith, N. E. Frattini, K. Serniak, P. Reinhold, I. M. Pop, S. Shankar, L. Frunzio, S. M. Girvin, and M. H. Devoret, Driving forbidden transitions in the fluxonium artificial atom, Phys. Rev. Appl. 9, 054046 (2018).

[18] U. Vool, I. M. Pop, K. Sliwa, B. Abdo, C. Wang, T. Brecht, Y. Y. Gao, S. Shankar, M. Hatridge, G. Catelani, M. Mirrahimi, L. Frunzio, R. J. Schoelkopf, L. I. Glazman, and M. H. Devoret, Non-poissonian quantum jumps of a fluxonium qubit due to quasiparticle excitations, Phys. Rev. Lett. 113, 247001 (2014).

[19] R. Shillito, A. Petrescu, J. Cohen, J. Beall, M. Hauru, M. Ganahl, A. G. Lewis, G. Vidal, and A. Blais, Dynamics of transmon ionization, Physical Review Applied 18, 034031 (2022).

[20] X. Xiao, J. Venkatraman, R. G. Cortiñas, S. Chowdhury, and M. H. Devoret, A diagrammatic method to compute the effective hamiltonian of driven nonlinear oscillators, arXiv preprint arXiv:2304.13656 (2023).

[21] M. Khezri, A. Opremcak, Z. Chen, K. C. Miao, M. McEwen, A. Bengtsson, T. White, O. Naaman, D. Sank, A. N. Korotkov, et al., Measurement-induced state transitions in a superconducting qubit: Within the rotating-wave approximation, Physical Review Applied 20, 054008 (2023).

[22] J. Cohen, A. Petrescu, R. Shillito, and A. Blais, Reminiscence of classical chaos in driven transmons, PRX Quantum 4, 020312 (2023).

[23] M. F. Dumas, B. Groleau-Paré, A. McDonald, M. H. Muñoz Arias, C. Lledó, B. D'Anjou, and A. Blais, Measurement-induced transmon ionization, Phys. Rev. X 14, 041023 (2024).

[24] D. Sank, Z. Chen, M. Khezri, J. Kelly, R. Barends, B. Campbell, Y. Chen, B. Chiaro, A. Dunsworth, A. Fowler, et al., Measurement-induced state transitions in a superconducting qubit: Beyond the rotating wave approximation, Physical review letters 117, 190503 (2016).

[25] K. N. Nesterov and I. V. Pechenezhskiy, Measurement-induced state transitions in dispersive qubit readout schemes, arXiv preprint arXiv:2402.07360 (2024).

[26] V. E. Manucharyan, J. Koch, L. I. Glazman, and M. H. Devoret, Fluxonium: Single cooper-pair circuit free of charge offsets, Science 326, 113 (2009).

[27] Note that the ground capacitances C_{g_n} are distinct from the self-capacitance $\frac{19.4}{E_{C,j}(\text{GHz})}$fF (see Table IV) across the junctions in the array, which set the junction array plasmon frequency [41].

[28] D. G. Ferguson, A. A. Houck, and J. Koch, Symmetries and collective excitations in large superconducting circuits, Physical Review X 3, 011003 (2013).

[29] G. Viola and G. Catelani, Collective modes in the

fluxonium qubit, Physical Review B **92**, 224511 (2015).

[30] In fact, the first four even parasitic modes with coupling strengths within a factor of 10 of $g_{\phi r}$. See Fig. 12 in App. B 1.

[31] T. N. Ikeda, S. Tanaka, and Y. Kayanuma, Floquet-landau-zener interferometry: Usefulness of the floquet theory in pulse-laser-driven systems, Physical Review Research **4**, 033075 (2022).

[32] We show that our results hold when simulated with 30 levels in the qubit mode and 10 levels in the parasitic mode.

[33] A relatively high-frequency choice, to reduce thermal, photon shot-noise induced dephasing in the qubit compared to lower-frequency bands.

[34] G. Zhu, D. G. Ferguson, V. E. Manucharyan, and J. Koch, Circuit QED with fluxonium qubits: Theory of the dispersive regime, Physical Review B **87**, 024510 (2013), publisher: American Physical Society.

[35] N. A. Masluk, *Reducing the losses of the fluxonium artificial atom* (Yale University, 2013).

[36] A. G. Fowler, M. Mariantoni, J. M. Martinis, and A. N. Cleland, Surface codes: Towards practical large-scale quantum computation, Physical Review A—Atomic, Molecular, and Optical Physics **86**, 032324 (2012).

[37] Z. Huang, P. S. Mundada, A. Gyenis, D. I. Schuster, A. A. Houck, and J. Koch, Engineering dynamical sweet spots to protect qubits from $1/f$ noise, Phys. Rev. Appl. **15**, 034065 (2021).

[38] M. D. Reed, L. DiCarlo, B. R. Johnson, L. Sun, D. I. Schuster, L. Frunzio, and R. J. Schoelkopf, High-Fidelity Readout in Circuit Quantum Electrodynamics Using the Jaynes-Cummings Nonlinearity, Physical Review Letters **105**, 173601 (2010), publisher: American Physical Society.

[39] M. H. Muñoz-Arias, C. Lledó, and A. Blais, Qubit readout enabled by qubit cloaking, Physical Review Applied **20**, 054013 (2023), publisher: American Physical Society.

[40] N. Didier, J. Bourassa, and A. Blais, Fast Quantum Nondemolition Readout by Parametric Modulation of Longitudinal Qubit-Oscillator Interaction, Physical Review Letters **115**, 203601 (2015), publisher: American Physical Society.

[41] G. Catelani, R. J. Schoelkopf, M. H. Devoret, and L. I. Glazman, Relaxation and frequency shifts induced by quasiparticles in superconducting qubits, Physical Review B **84**, 064517 (2011).

[42] J. Koch, V. Manucharyan, M. Devoret, and L. Glazman, Charging effects in the inductively shunted josephson junction, Physical review letters **103**, 217004 (2009).